ELSEVIER

Nuclear Instruments and Methods in Physics Research A 357 (1995) 418–442

NUCLEAR INSTRUMENTS & METHODS IN PHYSICS RESEARCH Section A

INDRA, a 4π charged product detection array at GANIL

J. Pouthas [a,*], B. Borderie [b], R. Dayras [c], E. Plagnol [a], M.F. Rivet [b], F. Saint-Laurent [a], J.C. Steckmeyer [d], G. Auger [a], C.O. Bacri [b], S. Barbey [b], A. Barbier [b], A. Benkirane [a], J. Benlliure [a], B. Berthier [c], E. Bougamont [c], P. Bourgault [a], P. Box [b], R. Bzyl [b], B. Cahan [c], Y. Cassagnou [c], D. Charlet [b], J.L. Charvet [c], A. Chbihi [a], T. Clerc [a], N. Copinet [a], D. Cussol [d], M. Engrand [b], J.M. Gautier [d], Y. Huguet [a], O. Jouniaux [e], J.L. Laville [d], P. Le Botlan [d], A. Leconte [d], R. Legrain [c], P. Lelong [b], M. Le Guay [a], L. Martina [a], C. Mazur [c], P. Mosrin [d], L. Olivier [a], J.P. Passerieux [c], S. Pierre [b], B. Piquet [a], E. Plaige [e], E.C. Pollacco [c], B. Raine [a], A. Richard [b], J. Ropert [a], C. Spitaels [a], L. Stab [c], D. Sznajderman [b], L. Tassan-got [b], J. Tillier [d], M. Tripon [a], P. Vallerand [a], C. Volant [c], P. Volkov [b], J.P. Wieleczko [a], G. Wittwer [a]

[a] *GANIL, BP 5027, 14021 Caen Cedex, France*
[b] *Institut de Physique Nucléaire, IN2P3-CNRS, 91406 Orsay Cedex, France*
[c] *CEA, DAPNIA, CE Saclay, 91191 Gif sur Yvette, France*
[d] *Laboratoire de Physique Corpusculaire, ISMRA, 14050 Caen Cedex, France*
[e] *Laboratoire de l'Accélérateur Linéaire, IN2P3-CNRS, 91405 Orsay Cedex, France*

Received 3 October 1994

Abstract

INDRA, a new and innovative highly segmented detector for light charged particles and fragments is described. It covers geometrically 90% of the 4π solid angle and has very low detection thresholds. The detector, operated under vacuum, is axially symmetric and segmented in 336 independent cells allowing efficient detection of high multiplicity events. Nucleus identification down to very low energy threshold (≈ 1 A MeV) is achieved by using ionization chambers operated with low pressure C_3F_8 gas. Residual energies are measured by a combination of silicon (300 μm thick) and cesium iodide (5 to 14 cm in length) detectors. Very forward angles are covered by fast counting phoswich scintillators (NE102/NE115). Charge resolution up to $Z = 50$ is achieved on a large energy dynamic range (5000 to 1 for silicon detectors). Isotopic separation is obtained up to $Z = 3$. The treatment of the signals is performed through specifically designed and highly integrated modules, most of which are in the new VXIbus standard. Full remote control of parameter settings, including visualization of signals, is thus allowed. The detector is continuously monitored with a laser source and electronic pulsers and is found stable over several days. Energy calibration procedures, making use of specific detectors and the ability of the GANIL accelerator to deliver secondary beams, have been developed. First experiments were performed in the spring of 1993.

1. Introduction

One of the main goals of the current research in nuclear physics in the intermediate energy domain is to improve our knowledge about the properties of nuclear matter at high density and temperature. Highly excited nuclear systems formed in heavy ion collisions can decay by emitting a large number of neutrons, "light particles" ($Z = 1$ or 2) and, to a lesser extent, heavier products ($Z > 2$) called "fragments". Several mechanisms may be at the origin of multi-fragment emission [1]. Of particular interest is the search for a "sudden multifragmentation" of the nuclei accompanied or not by a phase transition. This process is theoretically predicted to occur during the expansion of the hot and compressed system formed in the early stage of nucleus–nucleus central collisions [2–5]. Although the existence of multi-fragment emission is now well established, its nature and the underlying mechanisms are still poorly understood. Until recently, progress in the understanding of multifragmentation was partly hampered by the limitations of the available experimental devices. Indeed, the

* Corresponding author.

SSDI 0168-9002(94)01543-0

large number and the variety of particles and fragments emitted in central heavy ion collisions at intermediate energies require detectors with 4π solid angle coverage, high granularity, very low energy thresholds, large dynamic ranges in momenta or energies and identification capabilities on an event by event basis. In the last few years, a worldwide effort has been made in order to develop such detectors [6–12]. Taking advantage of the experience acquired with the first generation of 4π detection arrays, we undertook the construction of the INDRA detector ("Identification de Noyaux et Détection avec Résolutions Accrues") which is now installed at the heavy ion GANIL facility in Caen. Its characteristics were optimized for the study of heavy ion collisions with the beams and energies available at GANIL: from carbon to uranium at a maximum energy per nucleon decreasing with the projectile mass (from 95 A MeV for argon to 24 A MeV for uranium). The detector became operational at the end of 1992 and the first experiments were run in the spring of 1993.

Ideally, a 4π detector should provide, on an event by event basis, the number of particles in the event and, for each particle, give its identity (atomic number and mass), its energy (or velocity) and its emission angles (θ and ϕ). Detecting simultaneously neutrons and charged particles in a 4π geometry constitutes a real challenge and has not yet been attempted. INDRA has been specifically designed to detect charged products only. However its size was chosen so as to partially fit inside the GANIL neutron 4π detector ORION [13]. Measuring the mass of the fragments in a 4π geometry constitutes a major difficulty of its own. One method, which asks for the simultaneous measurements of the time of flight and of the energy of the fragments, requires large distances from the target and, although technically feasible, necessitates a huge size for the detector. Moreover, the mass identifications obtained are limited by the performances of the detectors which are commonly used [7]. An extension of this method to high resolution detectors over a large dynamic range was rejected as too expensive. Another method which has been adopted for the central part of the FOPI detector [11] consists in coupling energy loss measurements to a magnetic analysis in tracking chambers. However, the particles have to pass through the wall necessary to contain the gas inside the tracking chambers. This results in high energy detection thresholds which render this technique inappropriate at GANIL energies. Other 4π detectors [8–10] are based on scintillators such as CsI(Tl) for which the shape of the light pulse depends on the ionization density of the detected particle [14]. This method allows the detection and mass identification of light charged particles only ($Z = 1$ or 2). To overcome this limitation, a thin plastic scintillator is generally placed in front of the CsI(Tl) crystal [8–10]. The detector, thus operating as a phoswich, gives elemental identification instead of mass identification. However, this method leads to rather high energy thresholds and a maximum charge identification limited to $Z \approx 20$. Consequently, it was decided to use the well known properties of the CsI(Tl) crystal to determine the mass of H and He isotopes and to study the possibility of introducing, in a 4π array, detectors with high energy resolution such as ionization chambers (IoCh) and silicon detectors (Si) [15]. The identification of the fragments, limited to their atomic number, is obtained by the ΔE–E method applied to different detector pairs: IoCh–Si, IoCh–CsI and Si–CsI. The first detection layer composed of gaseous detectors (IoCh) gives the required low energy thresholds. Obviously, the detector design is more complex than one based only on scintillators and the main detection parameters and their limitations had to be carefully evaluated.

The two or three layer telescopes used in INDRA have an intrinsic possibility of satisfying nucleus identification and energy resolution requirements. However, the energy measurements must be performed on a large dynamic range as, for instance, from 1 MeV to 5 GeV for silicon detectors with an energy resolution of 100 keV. Such a performance could not be obtained by using conventional methods and commercially available electronic modules. As we had to design and build nearly all the electronics, we decided to mainly use a new standard, the VXIbus. VXIbus is an extension for analog processing of the VME computer bus (routinely used for data acquisition at GANIL). VXIbus allowed us to reduce considerably the number of modules by regrouping many functions in the same module. For instance, all functions related to 24 CsI(Tl) scintillators could be stacked in one module. It also provided the opportunity to locate all electronics close to the detector in the beam cave with full remote control (VXIbus/VME), including the display of analog and logic signals on oscilloscopes.

The detector parameters (granularity, geometry and choice of detection materials) are discussed in Section 2. The INDRA multidetector array is described in Section 3 and more details on the detectors are given in Section 4. The electronics and data acquisition will be presented in details elsewhere [16]. Section 5 gives an overview of their main features. The various energy calibration methods are discussed in Section 6. The performances of the detectors (mass and charge identification, energy dynamic range and homogeneity in detector responses) are presented in Section 7.

2. Main parameters of the INDRA detection array

2.1. Granularity

In the course of nucleus–nucleus collisions, particles and fragments are emitted in all directions. For the sake of simplicity, we will assume at first that these particles are emitted isotropically without any correlation. Assuming that the detector array covers the fraction Ω of the total

solid angle and that a number M of particles are produced in one event, the average number M_d of particles which will hit the array, irrespective of the number of detectors is simply given by:

$$M_d = M\Omega \tag{1a}$$

and the average number M_{loss} of particles missing the detector is:

$$M_{loss} = M(1-\Omega), \tag{1b}$$

whereas the probability $P(M)$ that the M particles hit the detector is given by:

$$P(M) = \Omega^M. \tag{1c}$$

Although the average number of detected particles in one event is directly proportional to the solid angle coverage, the probability of registering all particles decreases rapidly as the spatial coverage is reduced. The solid angle coverage is mainly dictated by mechanical constraints. For INDRA, the total loss of solid angle amounts to about 10% (see below, Section 3) which leads to $\Omega = 0.9$. Following the formalism of Refs. [17–19] and assuming that the array is divided into N_d equivalent detection cells with a 100% detection efficiency, the average number N_t of hit cells in an event containing M particles is given by:

$$N_t = N_d\left[1-(1-\Omega/N_d)^M\right], \tag{2}$$

whereas the probability $P(N_t = M)$ to have the number of hit cells equal to the number of particles (each particle hits a different cell) is given by:

$$P(N_t = M) = \frac{N_d!}{(N_d - M)!}\left(\frac{\Omega}{N_d}\right)^M. \tag{3}$$

This relation implies not only that all particles are detected but also that they are detected individually. Both quantities, N_t and $P(N_t = M)$ are related to the multi-hit probability P_{mult} (more than one particle in one cell) which is given by:

$$P_{mult} = \frac{1-(1-\Omega/N_d)^M - {}^1\left[1+(M-1)\Omega/N_d\right]}{1-(1-\Omega/N_d)^M}, \tag{4a}$$

which to a good approximation reduces to:

$$P_{mult} = \frac{(M-1)\Omega}{2N_d}, \quad \text{for } M < N_d/2 \tag{4b}$$

and thus is mainly governed by the ratio N_d/M. If each element of the array has a detection efficiency ϵ less than one, formulae (1) to (4) remain valid by replacing Ω with the product $\epsilon\Omega$. These relations can be generalized to the case of a non-isotropic particle emission pattern [18,19]. However, if the number of particles per detection cell is approximately uniform, they still hold to a very good approximation. Figs. 1a and 1b give respectively the average number N_t of hit detection cells and the probability $P(N_t = M)$ of detecting all particles individually as a function of the particle multiplicity M, assuming a 90% spatial coverage ($\Omega = 0.9$) and various granularities (different numbers of detection cells).

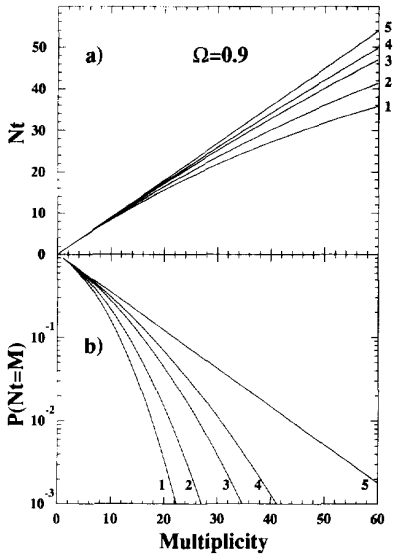

Fig. 1. (a) Average number N_t of hit detectors as a function of the particle multiplicity M. (b) Probability $P(N_t = M)$ to have the number N_t of hit detectors equal to the number of emitted particles as a function of the multiplicity M. The curves labelled 1, 2, 3, 4 and 5 refer to arrays covering 90% of 4π and made of 60, 96, 192, 336 and an infinite number of detection cells respectively. Isotropic and uncorrelated particle emission is assumed.

Obviously, the larger the number of elements in the array, the greater the probability of detecting all particles individually. However, this probability is limited by the total efficiency of the system (relation (1c)). For a given overall size of the detector, by increasing the number of elements, the dead layers between each cell tend to increase, thus decreasing the spatial coverage. Furthermore, the volume of the cells also decreases, favoring particle scattering from one cell to its neighbours. Thus the optimum configuration is a compromise between the size of the array and the number of its elements. With INDRA, the main criterion was to keep the multi-hit probability below 5%, which according to Fig. 2 leads to a ratio $N_d/M = 8$. At GANIL energies, the charged particle multiplicity is not expected to greatly exceed $M \approx 40$, leading to a division of the detector into about 320 elementary cells. On the other hand, the multiplicity of fragments is not expected to exceed $M \approx 10$. Thus, for those fragments, as long as they are distinguished from light charged particles, 80 detection cells are sufficient to keep the fragment multi-hit probability below 5%. Therefore, the first detection layer (IoCh), the purpose of which is to detect and to identify slow fragments, has been divided into 96 cells

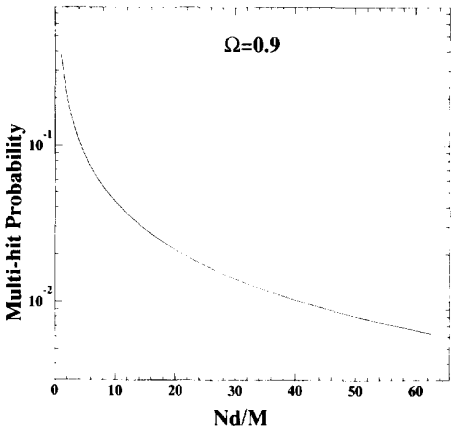

Fig. 2. Multi-hit probability as a function of the ratio of the number N_d of detection cells to the particle multiplicity M. Isotropic and uncorrelated particle emission is assumed.

whereas the subsequent layers (Si/CsI or CsI) are divided into 324 cells for the polar angles between 3° and 176°. The number of IoCh cells has been slightly increased in order to get a suitable mechanical arrangement of the array. For reasons which will be explained in the following, 12 cells were added to cover the angular range between 2° and 3°.

2.2. Geometry

The average particle azimuthal distribution is expected to be uniform around the beam axis which constitutes a natural symmetry axis. This led to a structure in rings centered on the beam axis. The arguments given in the previous section hold if the number of particles per detection cell is approximately uniform over the whole detector. In the laboratory, the velocity of the center of mass tends to focus the particles in the forward direction, producing a strong forward to backward asymmetry in the particle emission pattern. This focusing effect is stronger for reverse kinematics and is minimum for light projectiles impinging on heavy targets. The geometry of INDRA cannot be optimum for all projectile–target combinations, and in particular is not well suited for very asymmetric systems. INDRA has been segmented into 17 elementary rings centered on the beam. In order to accommodate kinematical focusing, depending on its polar angle coverage, each ring has been divided into 8,12,16 or 24 cells (see below: Section 3, Fig. 3 and Table 1). Furthermore, in

Table 1
Geometrical arrangement of the INDRA detectors. N: number of detectors per ring, e: thickness of detector, $\Delta\Omega$: solid angle of detector, n: number of CsI(Tl) behind an ionization chamber, d: distance from target, θ: polar angle, ϕ: azimuthal angle

Ring No.	Phoswich NE102–NE115 θ_{min} [deg]	θ_{max} [deg]	N	$\Delta\phi$ [deg]	e NE102 [mm]	e NE115 [mm]	$\Delta\Omega$ [msr]	d [cm]
1	2	3	12	30	0.5	250	0.37	130

Ring No.	CsI(Tl) θ_{min} [deg]	θ_{max} [deg]	N	$\Delta\phi$ [deg]	e [mm]	$\Delta\Omega$ [msr]	Si e [μm]	Ionization chamber $\Delta\phi$ [deg]	N	n CsI(Tl)	d [cm]	$\Delta\Omega$ [msr]
2	3	4.5	12	30	138	0.74	300	30	12	3	65.4	2.9
3	4.5	7	24	15	138	1.01	300					
4	7	10	24	15	138	1.70	300	30	12	4	38.4	10.3
5	10	14	24	15	138	3.21	300					
6	14	20	24	15	97	7.01	300	30	12	4	25	37.7
7	20	27	24	15	97	11.2	300					
8	27	35	24	15	90	15.8	300	30	12	4	12	86.0
9	35	45	24	15	90	26.4	300					
10	45	57	24	15	76	39.6	none	30	12	4	12	183
11	57	70	24	15	76	50.3	none					
12	70	88	24	15	48	81.0	none	30	12	2	12	155
13	92	110	24	15	60	82.3	none	45	8	3	12	240
14	110	126	16	22.5	50	93.5	none	45	8	4	12	338
15	126	142	16	22.5	50	73.1	none					
16	142	157	8	45	50	91.2	none	45	8	2	12	144
17	157	176	8	45	50	50.9	none					

order to keep reasonable cell sizes, rings 1 to 7 (forward angles) are located at decreasing distances from the target.

2.3. Detecting materials

Reaction products, issued from heavy ion collisions at GANIL energies, cover huge dynamic ranges, not only in energy (from ≈ 1 MeV to the maximum available energy of ≈ 6 GeV) but also in atomic number (from proton to uranium). Depending upon their energy and their atomic number, these particles or fragments will stop in a few μm or in several cm of detection material. For fragments identified by the ΔE–E method with an identification threshold of about 1 A MeV, the thickness of the first detection layer should not exceed an equivalent thickness of ≈ 6 μm of silicon. Furthermore, to identify fragments up to $Z = 30$, the energy resolution of this first detection layer should be better than 3% over an area of several cm^2. Gas ionization chambers which have been largely used in the past for this purpose seemed the only practical solution to this problem. They can be built in various geometrical configurations to match given experimental conditions and cover very large solid angles. Their effective thickness can be easily adjusted by changing the gas pressure or composition. The main challenge resides in the mechanical problem of minimizing the dead layers between cells and in paving the whole space with the best efficiency.

The largest energy dynamic range is encountered at forward angles (below 45°) where low energy particles and fragments issued from the target coexist with beam velocity particles and fragments from the projectile. These high velocity products deposit a very small amount of energy in the gaseous detectors and cannot be identified. For this reason, it was decided to introduce a second thin detection layer between 3° and 45°. This layer is made of 300 μm thick silicon wafers, each covering a gas ionization cell. Each wafer is divided into three or four independent fully depleted detectors. The maximum energy deposited in these detectors reaches ≈ 5 GeV whereas a high energy proton may deposit less than 1 MeV.

The last detection layer should be able to stop all particles and fragments and particularly high energy protons which have the longest ranges in matter. We chose CsI(Tl) crystals coupled to photomultiplier tubes. The use of photomultiplier tubes provides lower energy thresholds for mass identification as compared to those obtained with photodiodes [20]. The CsI(Tl) crystals combine the advantage of high stopping power, good energy resolution and the possibility of light particle isotopic identification by pulse shape discrimination techniques. One drawback of these detectors is the non-linear dependence of the light output on the energy of the incident particles which makes their calibration particularly delicate. In addition, for a given energy, the light output depends on the nature of the particle. For energy calibration purposes, rings 10 to 17 ($45° < \theta < 176°$) which do not incorporate silicon detectors were each equipped with a single two-element telescope (80 μm and 2 mm thick silicon detectors).

The first ring covering the polar angular range between 2° and 3° is often subjected to a high flux of elastically scattered particles and hence should be made of fast counting materials. This ring is made of 12 phoswich detectors each coupled to a photomultiplier tube. Each phoswich comprises a 500 μm thick plastic NE102 foil followed by a 25 cm long NE115 plastic scintillator.

3. Description and mechanical layout

To tackle the difficult problem of designing such a complex 4π detector, the whole mechanics of INDRA, including space required by electronics and connections, was computer designed [21]. Fig. 3 and Table 1 give the geometrical outline of INDRA. For the light particle detection, INDRA can be described as a series of 17 rings, each divided into a varying number of cells (from 8 to 24). In order to compensate for the forward peaked angular distributions, the solid angle subtended by each cell increases by a factor of 100 from forward to backward angles. For fragment detection, the space is divided in three regions:

– Ring 1 ($2° < \theta < 3°$) composed of 12 NE102/NE115 phoswiches,

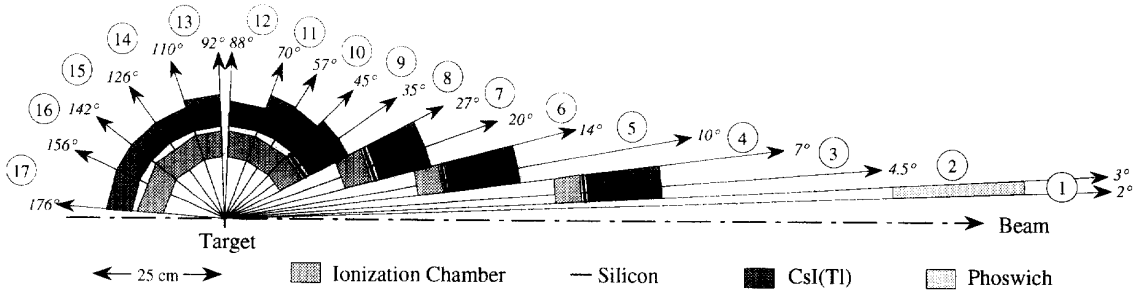

Fig. 3. Geometrical outline of the INDRA detector (cut along the beam axis). The detectors are arranged in 17 rings that are coaxial with the beam axis (see Table 1 for details).

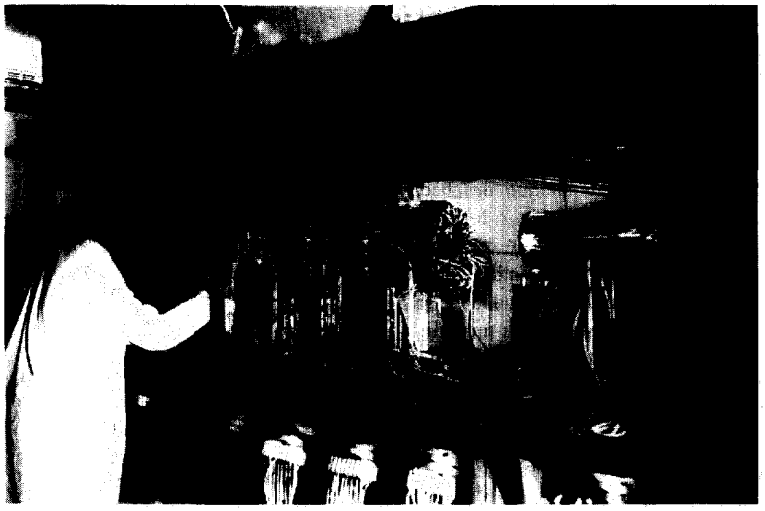

Fig. 4. Photograph of INDRA in its working position in the reaction chamber.

– Rings 2 to 9 ($3° < \theta < 45°$) composed of three successive detection layers: ionization chambers, 300 μm thick silicon detectors and CsI(Tl) scintillators. The silicon and the CsI(Tl) detectors have the same geometry whereas an ionization chamber cell covers 3 or 4 silicon detectors on two adjacent rings (see Table 1).

– Rings 10 to 17 ($45° < \theta < 176°$) composed of ionization chambers and CsI(Tl) scintillators in an arrangement presented in Table 1 (an ionization chamber cell for 2, 3 or 4 CsI(Tl) scintillators, depending on the ring number). Each of these rings is equipped with a calibration telescope composed of a 80μm thick silicon detector and a 2 mm thick lithium ion-drift silicon detector.

To summarize, INDRA is composed of 12 NE102/NE115 phoswiches, 96 ionization chambers, 180 silicon detectors, 324 CsI(Tl) scintillators and 8 silicon calibration telescopes in an arrangement which geometrically covers 90% of the 4π solid angle. The loss of solid angle amounts to 0.2% for the beam entrance and exit ports, 3.5% for the target holder region ($88° < \theta < 92°$) and 6.3% for the ionization chamber walls.

A photograph of INDRA is shown in Fig. 4. In its running configuration, the detector is 200 cm long with a maximum outside diameter of 80 cm. The detector is housed in a dedicated vacuum vessel with a removable cover giving easy access to all detector elements and

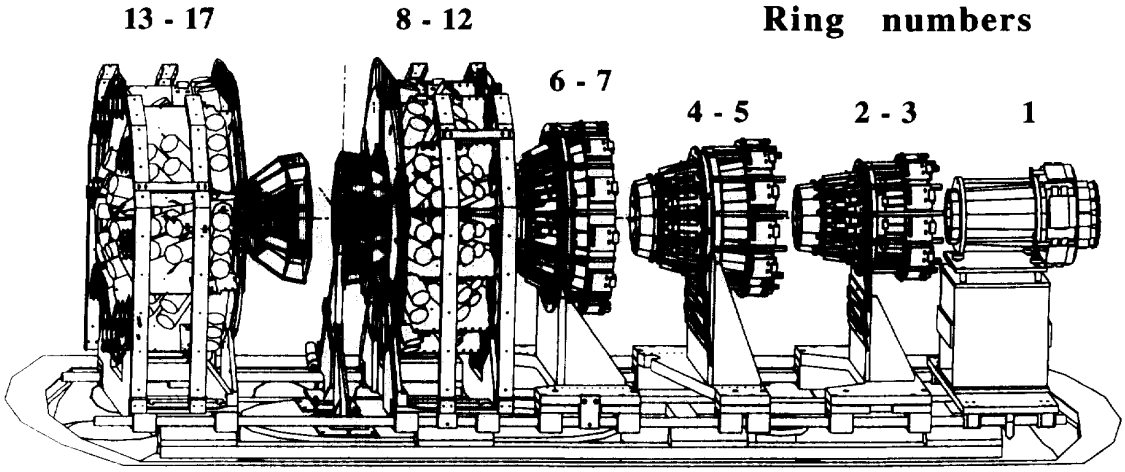

Fig. 5. Split view of INDRA. The six carriages which support the detectors are separated. The two ionization chamber arrays (rings 8 to 12 and rings 13 to 17) are presented out of their supports.

connections (see Fig. 4). The different parts of the detector are supported by six carriages which can slide independently on two rails (Fig. 5). From forward to backward angles, the carriages support respectively ring 1, rings 2 and 3, rings 4 and 5, rings 6 and 7, rings 8 to 12 and rings 13 to 17. The target holder is inserted between these two last carriages. The same assembling technique has been adopted for rings 2 to 7 and is illustrated in Fig. 6 for rings 4 and 5. The ionization chamber structure can be easily removed from its support. Each ionization chamber cell is followed by a silicon wafer supporting 4 independent detectors and a group of 4 CsI(Tl) crystals each matching in size the corresponding silicon detector. This configuration optimizes the geometrical efficiency by minimizing dead areas between detectors. For a given cell, the preamplifiers (1 for the ionization chamber and 4 for the silicon detectors) are mounted on a single multilayer printed circuit board located on the outside wall of the CsI(Tl) scintillator support, thus reducing the connection length to the detectors. For rings 8 to 17 which surround the target at a fixed distance of 12 cm, a different assembling technique had to be used. The ionization chambers consist of two independent mechanical structures of 36 cells and 24 cells for rings 8 to 12 and rings 13 to 17 respectively. Obviously, the construction of these structures and the connections to the electronics are more complex. Fig. 7 shows the detectors, the electronics and the connections of rings 8 to 12. The 120 photomultiplier bases are placed as close as possible to the photomultipliers. The 36 ionization chamber preamplifiers by groups of 6 and the 6 calibration telescope preamplifiers (rings 10 to 12) are located at $\theta = 90°$. The 48 preamplifiers associated with the silicon detectors could not be placed as close to the detectors as in the forward rings and were positioned at the edge of the mechanical structure, 20 cm away from the detectors. Strip-line printed circuit boards of 0.4 mm total thickness insure the connections.

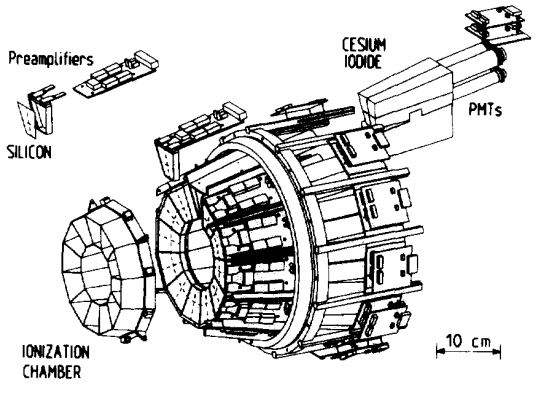

Fig. 6. Detector assembly for rings 4 ($7° < \theta < 10°$) and 5 ($10° < \theta < 14°$). The ionization chamber is a 12 cell array. The 48 CsI(Tl) scintillators are assembled in 12 sets of 4 pieces each. The silicon detectors have a geometry identical to the one of the scintillators: 4 pads are designed on the same wafer. The preamplifiers are located on the external wall of the CsI(Tl) support.

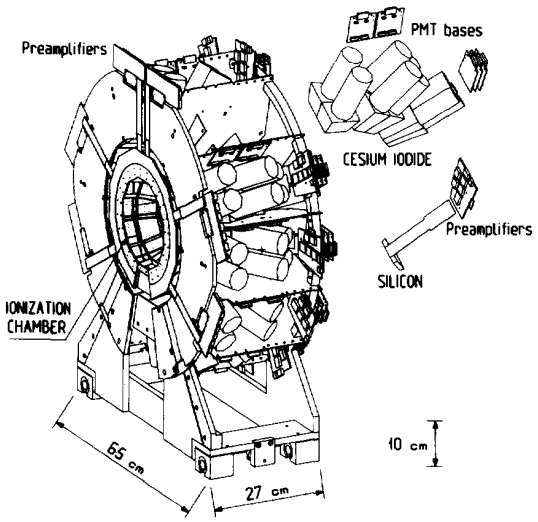

Fig. 7. Detector assembly for rings 8 to 12 ($27° < \theta < 88°$). A selected group of detectors covering $\Delta\Phi = 30°$ and the associated electronics (10 PMT bases by groups of 2; 4 silicon detector preamplifiers mounted on a unique multilayer printed circuit board) are shown removed from the mechanical support. The 36 ionization chamber preamplifiers are grouped by 6 and located at $\theta = 90°$.

In order to avoid cross-talk between the photomultiplier bases and the preamplifiers (particularly the high gain preamplifiers of the ionization chambers), the latter have to be shielded. The ground shields are also used to remove, by water cooling, the excess heat (≈ 120 W) generated in the 292 preamplifiers. Without cooling, temperature in excess of 50°C are reached on the mechanical support of the CsI(Tl) crystals affecting their light output which critically depends on the temperature [22]. After 10 hours of water circulating at 10°C, the temperature stabilizes around 20°C on the mechanical supports of the CsI(Tl).

4. Detectors

4.1. The gas ionization chamber array

The first INDRA detection layer ($3° < \theta < 176°$) is composed of 96 gas ionization chambers. Here, the difficulties come from trying to cover the whole space with gas cells with an efficiency close to 1 and ensuring an independence of the signal with position. This was achieved by choosing gas counters with a specific axial field design. The ionization chambers are 5 cm thick and operate at low gas pressure (less than 60 mbar).

The mechanical structure of the gas ionization chambers for rings 4 and 5 is shown in Fig. 8. The structure is made in one piece by fiberglass casting. Each structure is divided in twelve identical cells. Each cell has the shape of a truncated pyramid, 5 cm high, with the entrance and exit faces tangent to two spheres centered at the target position. The inner and outer walls are 1 mm thick whereas the partition walls are 0.8 mm thick. After casting, 0.1 mm thick printed circuit boards bearing 1.5 mm broad copper strips separated by 2.5 mm are glued on the 4 side-walls of each cell in order to obtain 11 rings for field shaping. The first and last rings are located at 4.25 mm from the entrance and the exit of the cell respectively. The last ring is connected to a grid which is common to all cells. This grid located at 5 mm from the exit of the cells is made of 50 μm Cu–Be wires which are placed every 5 mm and thus ensures a 99% transparency. Before weaving the grid, two holes were drilled in all but one of the partition walls in order to ensure gas circulating between cells. Gas inlet and outlet are located on the two adjacent cells with a non-bored partition-wall. In each cell, the first field shaping ring is connected to the cathode through a 10 MΩ chip resistor, rings 1 to 9 are interconnected through 10 MΩ chip resistors whereas a 20 MΩ chip resistor connects ring 9 to ring 10 which in turn is connected to ring 11 (the grid) through a 51 MΩ chip resistor. The grid itself is grounded through a 10 MΩ resistor and a 10 nF capacitor. The most delicate part in the assembling process was to mount the electrodes on the mechanical structures. The cathode (entrance window) which is common to all cells is made of a 2.5 μm mylar foil aluminized on one side and glued onto the entrance face of the structure. Each cell required an anode electrically insulated from its neighbours. In order to achieve this, a brass mask was cut out by chemical etching and matched the 12 cells on the exit face. This mask was then used to make the twelve anodes simultaneously by evaporating aluminum on a 2.5 μm mylar foil. This foil, after a careful positioning, was glued on the exit face of the mechanical structure. The anodes were then connected cell by cell, using conducting glue, to a microconnector in order to facilitate the coupling to the preamplifiers PCB (printed circuit board) (see Fig. 6). The same technique was applied in the construction of the ionization chambers for rings 2 and 3 and rings 6 and 7.

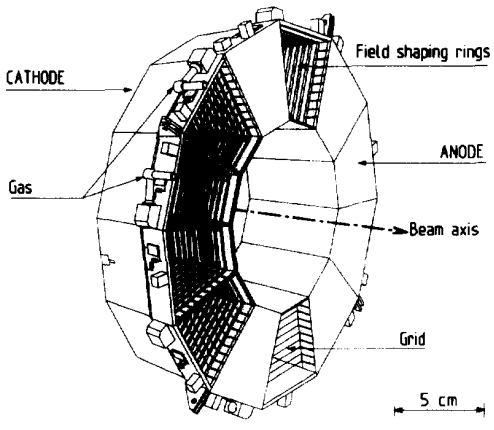

Fig. 8. The ionization chamber array (12 cells) of rings 4 and 5. A part of the anode foil is removed to show the grid and the field shaping rings inside the cells.

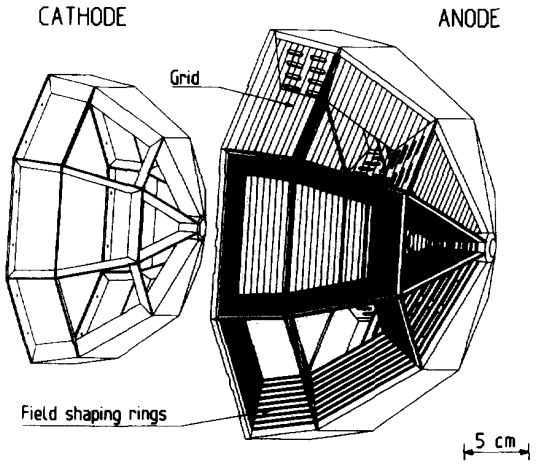

Fig. 9. The ionization chamber array (24 cells) of rings 13–17. The two separated structures supporting the anodes and the cathodes are presented before mounting. Foils are removed to show the mechanical structures and the inside of the cells.

Fig. 9 shows the composition of mechanical structures used in the ionization chamber array for rings 13–17. Two separate structures supporting the anodes and the cathodes of the ionization chambers before mounting are presented. The anode structure contains the walls which separate the 24 cells. Due to the complexity of these structures, casting seemed impracticable and they were made by using multilayer PCBs glued together. Each PCB was constructed with a precision of 0.01 mm and its placement was accurate to 0.1 mm. These boards are used to carry the signals from the anode to the back of the structure where they can be connected to the preamplifiers. The field shaping rings are interconnected between cells and thus, a single resistor chain gives the same field distribution as in rings 4 and 5. As there is only one gas inlet and outlet, particular care was taken in positioning the holes in the partition walls to ensure a good circulation of the gas. Contrary to rings 2 and 3, 4 and 5, and 6 and 7, the electrodes could not be glued on in one piece and had to be split into 8 slices. The ionization chamber array of rings 8–12 was built along the same lines.

The operating conditions were defined using test cells of the same design as those of INDRA. First attempts were made to operate cells without the grid in order to avoid particle scattering from the grid wires. Although such cells

had a good resolution locally, it was found that the anode signal increased by about 10% when the trajectories of the impinging particles moved from the axis of the cell towards its edges, and so deteriorating its overall resolution. Calculations of the electric field within the cell showed that the field was non-uniform and distorted in the vicinity of the anode. To correct these effects, a grid as previously described was introduced to render the response uniform within 1% over the whole cell. To avoid unsticking of the electrodes from the structure, the operating pressure is limited to about 60 mbar for the three forward arrays (rings 2 to 7) and to about 50 mbar for the two others (rings 8 to 17). Typically, the ionization chambers of rings 2 to 7 are operated at 50 mbar and those of rings 8 to 17 at 30 mbar of high purity perfluoropropane (C_3F_8). Apart from being nonflammable and nontoxic, this gas was chosen for its high molecular weight ($A = 188$). Under the same operating conditions, it delivers pulses twice as large as CF_4 with a collection time for the electrons being about twice as long [23]. In order to maintain its properties, the gas circulates continuously and is entirely renewed every 20 minutes. Full charge collection is attained for electric field strengths of 0.9 V $cm^{-1}mbar^{-1}$ and 7 V $cm^{-1}mbar^{-1}$ in the cathode–grid and grid–anode spaces respectively. These electric fields are sufficiently low so as to avoid any high voltage breakdown. The anodes are directly connected to very high sensitivity charge preamplifiers (0.25 pF feedback capacitor equivalent to 200 mV/MeV for silicon detectors). With C_3F_8 gas, these preamplifiers deliver pulses with amplitude of 20 mV/MeV.

4.2. The silicon detectors

As previously discussed, 180 silicon detectors, 300 μm thick, are placed on rings 2 to 9 ($3° < \theta < 45°$) (see Table 1). In order to minimize the dead zones resulting from the mechanical supports, 3 or 4 pads were designed on the same wafer whose external dimensions correspond to the ionization chamber cell. This results in 48 wafers which are classified in 4 groups of 12 elements. Each has a trapezoidal shape whose total active area and number of pads depend on the rings: 14 cm^2 (3 pads), 19.8 cm^2 (4 pads), 34.5 cm^2 (4 pads) and 26.8 cm^2 (4 pads) for rings 2 and 3, 4 and 5, 6 and 7, and 8 and 9 respectively. The silicon detectors were made by Intertechnique [24] using the planar process. The photolithography of the process [25] provides the possibility of extending the sensitive area of the detector up to the edges of the wafer. Nevertheless, a border, 0.7 mm wide, was preserved on the outside of the pads in order to avoid large current flows and breakdown effects on the wafer edges when the detectors are biased.

In order to avoid cross-talk effects due to the capacitive coupling between the ionization chamber anode and the silicon detectors placed just behind (and bearing in mind that 6 mm corresponds to a few pF depending on the detector area), the side of these detectors facing the ionization chamber must be grounded. As the pads are necessarily designed on the p^+ side, the grounded side must be the n^+ one and consequently the particles enter the detectors by the low electric-field side. Evidently, the detector must be fully depleted and, if possible, overbiased. The field strength of an overbiased detector varies linearly from a minimum F_{n^+} on the n^+ side to a maximum F_{p^+} on the p^+ side: $F_{n^+} = 10(V_b - V_0)/d$ and $F_{p^+} = 10(V_b + V_0)/d$ where V_b (in V) is the bias voltage, V_0 (in V) is the depletion voltage and d (in μm) is the detector thickness, F is then in units of kV/cm. A high value of F_{n^+} is obtained with a low depletion voltage V_0 and a high bias V_b. The use of high resistivity silicon provides low values for V_0 since the depletion voltage can be expressed by $V_0 = 4 \times 10^{-3}\ d^2/\rho$ where ρ is the silicon resistivity in kΩ cm. A high resistivity also gives a smooth variation of the electric field strength across the detector and, overall, the moderate maximum field reached on the p^+ side is still compatible with a thin edge detector design.

Studies making use of radioactive sources (6.05 MeV and 8.78 MeV α particles from $^{212}Bi/^{212}Po$ and fission fragments from ^{252}Cf) were performed on a first set of 4 detectors to determine the effects of overbiasing [26]. Unfortunately, all the INDRA detectors could not be largely overbiased and the effects of the bias voltage on the energy measurements had to be tested. The detectors of ring 2 were checked by using elastically scattered ^{84}Kr ions of 35 A MeV on a gold target. These ions deposit 1250 MeV in the silicon detector. The bias voltage was varied around the depletion value (40 V) from 20 to 80 V. The charge preamplifier rise times were observed for a set of 4 detectors while energy measurements were performed on the 8 other ones. Fig. 10a presents the rise time (10%–90%) versus the detector bias voltage. The four detectors tested give similar results. The pulse rise at the preamplifier output was approximated by an exponential variation with respect to time: $1 - \exp(-t/\tau)$. The values of τ are also given in Fig. 10a. The energy measurements were performed with the INDRA electronics [16]. The energies measured with a detector bias of 80 V are taken as the reference points. Fig. 10b gives the relative variation for the two detectors which presented the most extreme variations as a function of the bias voltage. The ballistic deficit of the electronics calculated for the rise time observed is also presented in the same figure. To within the exponential approximation, the results of these calculations are consistent with the experimental data. The low ballistic deficit of the INDRA electronics which is around ten times better than the one of the chains based on spectroscopy amplifiers and peak sensing ADCs [16], explains the observation that the energy measurements are little affected by the slow collection times (up to 1 μs and even more). Hence, the "charge collection" must be relatively important, even for detectors which are not fully depleted. The

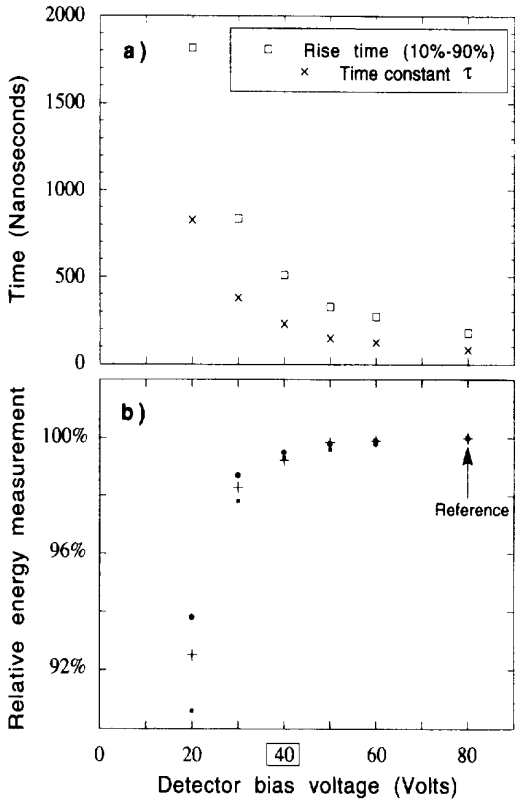

Fig. 10. (a) Charge preamplifier rise times (10%–90%) of an INDRA silicon detector (ring 2) irradiated by 35 A MeV krypton ions (1250 MeV deposited in the detector) for different detector bias voltages. The depletion voltage is 40 V and τ is the time constant derived from an exponential time variation assumption. (b) Relative variations of the energy measured with the INDRA electronic chain. The energy measured at 80 V bias is taken as the reference. The measurements have been performed on 8 detectors of ring 2. Circles and squares show the results for the detectors which have presented the smallest and the largest variations. Crosses (+) refer to the electronic ballistic deficit calculated for the observed rise times assuming an exponential time variation.

detector responses were evaluated at very low bias voltages by observation of the preamplifier pulse amplitudes. The "charge collection" is around 87% (with a rise time of 4 μs) and more than 60% (with a rise time of 15 μs) of the one observed at $V_b = 80$ V, respectively for $V_b = 10$ V and $V_b = 0$ V. These results cannot be explained by models in which the "charge collection" relies mainly on the density distribution of the ionized track in relation to the field strength in the detector. In the hyperpure silicon used in planar technology, the minority carrier lifetime is greater than a few milliseconds [27] and other mechanisms, such as carrier diffusion, must be considered. Moreover, the resistivity given by the manufacturer is only a mean value and resistivity variations in the detector bulk [27] could give different results for detectors having the same nominal characteristics [28]. Nevertheless, a relatively fast collection (15 μs) of more than 60% of the charge is still difficult to understand and certainly implies that dynamical effects, in relation to the primary ionization in the wake of the impinging ion, need to be introduced. The literature on field-free transport (charge funnelling and charge migration in quasi-neutral silicon) is critically reviewed in Ref. [29] and a new mechanism based on the action of the high–low (n^+n^-) junction is suggested to explain the surprisingly fast charge collection for particles impinging the detector by the n^+ side. Whatever the explanation may be, our experiments show that the measurement of the energy deposited by krypton ions can be performed even if the detector is not overbiased, provided they are not stopped within the detector. Conversely, a pulse height defect (PHD) [30] still exists for heavy ions which stop in the detector, even if reduced by the quality of the silicon and of the electronics (low ballistic deficit). Energy calibration and PHD results are given in Section 6. In summary: i) we use high resistivity silicon of around 10 kΩ cm, or more, with a long carrier lifetime of a few ms, ii) when possible, the detectors are overbiased to 2 or 3 times the depletion voltage, iii) the electronics have a low ballistic deficit in order to obtain energy measurements that are nearly independent of the large rise-time variations in the detector signals.

Fig. 6 shows how the detectors in rings 4 and 5 are mounted. The silicon wafer is held by a support made of four multilayer PCB glued together. Three of the sides are 0.8 mm thick. As it does not introduce geometrical cuts, the side nearest the preamplifiers is thicker (6 mm) and ensures the rigidity of the support. Two PCB complete the support and are screwed on the preamplifier motherboard. The assembly is the same for rings 2 and 3, and 6 and 7, but slightly different for rings 8 and 9 where 20 cm long strip-line circuit boards had to be implemented (Fig. 7). The preamplifiers are located as close as possible to the detectors: a few centimeters on rings 2 to 7 and 20 cm on the rings 8 and 9. The main characteristics of the charge preamplifiers are: a sensitivity of 2 mV/MeV, an output dynamic range of 10 V and an intrinsic resolution of 14 keV for a 200 pF detector capacitance. The preamplifiers have been studied and individually checked in order to have the same gain within ±1%, an interesting feature for energy response comparisons and calibration purposes.

4.3. The CsI(Tl) scintillators

For the 324 CsI(Tl) crystals, 30 different shapes are used. The front and back faces of the crystals are polished. The sides and the free part of the back face are wrapped first of all with a diffusing material (120 μm white teflon tape) and then with an aluminized mylar foil (5 μm mylar and 20 $\mu g/cm^2$ aluminum) to avoid light leakage. The front face of each scintillator is covered with a very thin

evaporated aluminum layer ($30\mu g/cm^2$) and the back face is glued (with optical EPO-TEK 302) to the front window of the photomultiplier tube (PMT). To simplify the mechanical assembly, we decided not to use light guides between crystals and PMTs. The effects of the absence of light guides were checked through measurements and simulations. The response of a prototype detector (8 cm long) to collimated protons of various energies (21, 141 and 159 MeV) impinging on two different areas was studied (Fig. 11). Protons of 21 MeV were delivered by the CYCLONE cyclotron at Louvain-la-Neuve and protons of 141 and 159 MeV by the ORSAY Synchrocyclotron using a magnetic spectrometer. Fig. 11b shows the evolution of the light response for region 2 normalized to the light for region 1. We observe a decrease of the light response only when protons of 159 MeV, which have a 7.1 cm range in CsI(Tl), are detected. The result of a simulation performed with the GUIDE7 program [31] is also indicated and agrees rather well with the experimental results. From these results and from simulations for different PMT diameters and positions on different back faces, an increase of the length initially proposed was decided in order to mimic a light guide. Depending on the ring, 1.7 to 2 cm were added. Table 2 gives the maximum energy of light particles stopped in the crystals and the maximum energy of particles whose range is equal to the crystal length minus two centimeters. The second set of values can be considered as the maximum light charged particle energies for which the CsI(Tl) crystals give energy measurements independent of position.

Special care was taken to select CsI(Tl) crystals of uniform scintillation efficiency. This was done by scanning, in air, each crystal along its length (3 to 7 measurements, depending on the length) with collimated γ-rays from a ^{137}Cs source. For these tests, the sides of the CsI(Tl) crystals were wrapped with their final materials and the front face was covered with an aluminized mylar foil. The back face of the crystal was located 3 mm from the front window of a PMT of 76 mm diameter (Philips XP 3461B). The collimated source was arranged so as to irradiate less than 1 cm along the length. Standard electronics (an amplifier with 2 μs shaping constants and a peak sensing ADC) was used to analyze the PMT signal. In order to estimate the variation of light outputs with the

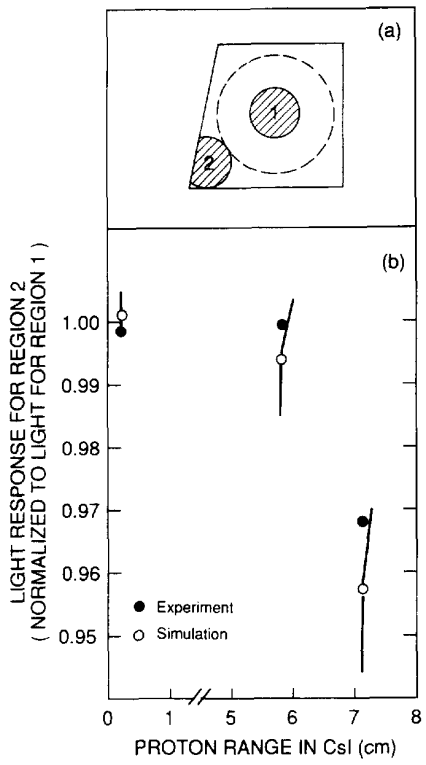

Fig. 11. Light response as a function of proton tracks for a prototype CsI(Tl) detector, 8 cm long. (a) Back face of the crystal; the dashed circle delimits the PMT position (diameter: 38 mm) and regions 1 and 2 are the projected zones (diameter: 15 mm) of collimated proton tracks. (b) Evolution of the light response for protons of different energies impinging on region 2 (normalized to the light for region 1). Experimental results correspond to full circles. Open circles refer to simulations (GUIDE 7 program): error bars from simulations are deduced from a sampling which mimics the collimated region.

Table 2
Maximum detected energy of light particles in the CsI(Tl) detectors. The values in brackets give the energy of particles whose range is equal to the crystal length minus 2 cm (see text)

CsI(Tl) detectors		Maximum energy [MeV]				
Rings	Thickness [mm]	^1H	^2H	^3H	^3He	^4He
2 to 5	138	237 (215)	313 (285)	370 (337)	847 (770)	948 (862)
6 and 7	97	192 (167)	255 (223)	300 (263)	683 (594)	766 (668)
8 and 9	90	183 (158)	244 (210)	288 (249)	654 (552)	733 (632)
10 and 11	76	166 (138)	221 (185)	262 (220)	591 (493)	664 (554)
12	48	126 (92)	169 (123)	199 (145)	448 (328)	504 (368)
13	60	144 (113)	192 (152)	228 (180)	512 (404)	577 (453)
14 to 17	50	129 (96)	173 (128)	205 (152)	460 (340)	517 (384)

different crystal shapes, simulations of the measurements were performed with the GUIDE7 program. Selected crystals had to satisfy the following specifications:

–a very low phosphorescence after exposition to normal daylight. The height of the 662 keV photoelectric peak of a cesium source had to exceed the background level by a factor 40 after 10 min in obscurity.

– a scintillation efficiency constant to within 5% along the whole length.

– average light outputs within a 15% tolerance for all the crystals of the same ring.

– an average light output varying from 70% (ring 2) to 170% (ring 15), taking ring 5 as a reference.

Using two identical set-ups for the measurements, all of these specifications were independently checked by both the manufacturer [32] and the laboratory in charge of the CsI(Tl) detectors.

A good match to the geometrical shapes of different crystal back faces was obtained by using PMTs with four different diameters: 19, 29, 38 and 51 mm. These PMTs were chosen for their high stability and linearity. Specification requirements are summarized in Table 3. To meet these requirements, Philips Photonics [33] proposed the 10-stage models XP2081 (38 mm) and XP2201 (51 mm) and developed for the INDRA project two new 8-stage models: XP1981 (19 mm) and XP2961 (29 mm). The manufacturer checked dark current, luminous sensitivity and linearity and all the stability tests were performed at reception on a semi-automatic computer controlled test-bench. All PMTs, grouped in batches of 12, were tested for stability during two days, after 32 h ageing, and at a temperature constant within 3°C. Light pulses (with rise time = 500 ns and decay time = 1 μs) were provided by LEDs (HP 5082–4950 green GaP) and a very stable PMT was used to monitor the overall system stability. Typical test results are shown in Fig. 12.

Each PMT is surrounded by a cylindrical μ-metal shield which is isolated from the photocathode and grounded to avoid cross-talk with the neighbouring ionization chamber preamplifiers. The photomultiplier bases work under vacuum and, in order to minimize power consumption, specific bases were developed. Transistorized switches

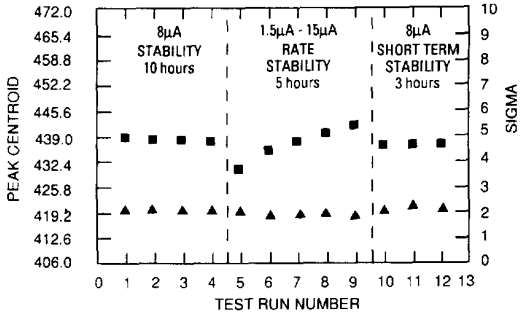

Fig. 12. Example of a photomultiplier tube (XP1981, 19 mm diameter) test result after ageing (32 h, $\langle I_a \rangle = 8$ μA). Test runs 1–4 refer to stability, test runs 5–9 to rate stability and tests 10–12 to short term stability (see Table 3). Squares correspond to the peak centroid position and triangles to sigma values.

ensure a fast replenishment of the capacitors associated with the last dynodes. These transistorized bases dissipate 10 times less power and recover 30 times faster than their resistor-only (or RC) counterparts [16]. In rings 2 and 3, where elastically scattered heavy ions of a few GeV can be expected, the base current is 150 μA while an average current of 75 μA is enough in the PMT bases of the other rings. Such low currents lead to a power consumption which does not need a specific base cooling system.

4.4. The NE102 / NE115 scintillators

The first ring ($2° < \theta < 3°$) is composed of 12 plastic phoswich detectors [34]: a fast plastic (NE102, $\tau = 2.4$ ns) [35] with a thickness of 500 μm and a slow plastic (NE115, $\tau = 240$ ns) [36] with a thickness of 25 cm. The two plastics are glued together with optical cement [35]. The PMTs (Philips Photonics XP2982, 29 mm diameter) are directly glued on the back face of the slow plastic. To improve the light collection, an aluminized mylar foil (0.15 mg/cm^2) covers the front face of each phoswich detector, and the polished tapered sides are wrapped with white teflon tape and aluminum foils. The PMTs are surrounded by a cylindrical μ-metal shield. Typical gain

Table 3
Characteristics required for the photomultiplier tubes associated with the CsI(Tl) crystals

Gain range for the different PMT diameters	19 mm: 3.10^4–3.10^5 29 mm: 3.10^4–3.10^5 38 mm: 7.10^4–7.10^5 51 mm: 10^5–10^6
Dark current at gain 10^5 and 20°C	< 50 nA
Luminous sensitivity (green extended photocathode)	> 100 μA/lm
Linearity deviations, over the range 0–60 mA, $\langle I_a \rangle$ = 0–3 μA at minimum values of the gain range (pulse width: 500 ns)	< 2%
Stability, maximum variation of gain during 10 h, $\langle I_a \rangle = 8$ μA	< 3%
Rate stability, maximum variation of gain when $\langle I_a \rangle$ changes from 1.5 μA to 15 μA	< 5%
Short term stability, maximum variation of gain during a series of 25 s cycles (20 s: $\langle I_a \rangle = 8$ μA; 5 s; $\langle I_a \rangle = 0$)	< 5%

values are around 5×10^5. The transistorized photomultiplier bases specifically developed for INDRA are used to reduce power consumption. For this ring, the base current is ≈ 200 μA.

Tests have been performed with fast scintillators of different thicknesses and the thickness of 500 μm was selected [37]. It allows a good Z identification with moderate thresholds: 6.3 A MeV for $Z = 1$ and 2 particles, 20 A MeV for ^{40}Ca ions and 23 A MeV for ^{84}Kr ions. The slow scintillator, 25 cm in length, stops protons up to 200 MeV. Since the transverse section of the scintillator is small compared to its length, it was checked that losses due to angular straggling remained at a low level. Assuming a uniform energy distribution up to 200 MeV, simulations performed with the GEANT code [38] showed that the fraction of H nuclei escaping from one detector is less than 1.3%.

4.5. The calibration telescopes

It is well known that the energy calibration of CsI(Tl) scintillators is a difficult task, since, for a given energy, their light response is Z and A dependent and moreover is non-linear for a given species [10]. A direct calibration of INDRA scintillators is possible for light charged particles by using elastically scattered secondary proton and alpha beams (see Section 6). However, in the case of heavier fragments, this method is unmanageable. It was therefore decided to use the energy loss in the 300 μm silicon detectors at forward angles and to equip rings 10 to 17 with calibration silicon detector telescopes inserted between the ionization chamber and the scintillator. Due to the axial symmetry of INDRA, one telescope per ring is sufficient to obtain reference spectra provided the chosen trigger does not break the symmetry. The calibration telescopes comprise a 80 μm thick silicon detector followed by a 2 mm thick Si(Li) (lithium ion-drift silicon detector). These detectors were manufactured at the IPN Orsay laboratory. They are all 1 in. diameter circular wafers and therefore smaller than the CsI(Tl) crystal located behind them.

The 80 μm detectors are of the surface barrier type [39]. A tin oxide layer, 20 nm thick, is deposited on the wafer surface before the 35 nm gold electrode evaporation. This ensures stability against changing ambient conditions while avoiding the use of varnish or epoxy for edge protection. The back aluminum electrode is 100 or 200 nm thick, depending on the detector. The active area of the detectors is 380 mm^2. This corresponds to a dead zone of 1.7 mm at the edges. The bias applied to these detectors was chosen on charge collection criteria. It was increased up to the point where the response of the detectors to ^{241}Am α saturates. The bias thus obtained is 12 V larger than the value calculated for full depletion (8 V).

The Si(Li) detectors, 2 mm thick, do not stop energetic protons and α particles. To obtain correct energy measurements for such particles, it is necessary to minimize the Li window located at the back face of the detectors. Windows as thin as 40 μm were obtained. The thickness of this dead layer was measured in two ways:

– Firstly by using 8.78 MeV α from a ^{212}Po source impinging successively on the front and the back face of the detector; the difference in the energy response gives the thickness of the Li layer.

– Secondly by means of energetic protons: one INDRA detector and a 4 mm Si(Li) detector were separately calibrated with 10 and 15 MeV protons delivered by the CYCLONE cyclotron at Louvain-la-Neuve. A precision pulser monitored the stability of the electronic chains. The INDRA detector was mounted in front of the 4 mm Si(Li) and irradiated by 30 MeV protons. The sum of the energies measured in the two detectors amounted to 29.81 MeV. The missing 190 keV were attributed to the rear dead layer of the 2 mm detector which was evaluated at a thickness of 43 ± 11 μm. This value is in excellent agreement with the 44.2 μm found with the previous method on the same detector.

With the same proton beam, we measured the residual energy in the second detector while moving a 5 mm collimator in front of the telescope. This gave the thickness of the 2 mm wafer along a diameter. The homogeneity is excellent, the thickness of the detector was found to be equal to 2247 μm with a dispersion, $\sigma = 3$ μm. The second constraint for these detectors, used in a 4π environment, is the minimization of the inactive zone on the edges of the wafer. A careful study of this problem allowed us to reduce this zone to 0.7–1 mm (this corresponds to the difference between the wafer and the Li window radii). Both the front and back electrodes are gold layers of 35 nm thickness (barrier face) and 20 nm (back).

The mechanical frame of the telescope is constrained by minimal shadowing of the 4π geometry. Fig. 13 presents the mechanical assembly of the 8 telescopes and their position in front of the CsI(Tl) crystals. Both detectors are fixed on a 0.5 mm thick aluminum oxide ring. The inner ring diameter between the two detectors is 23.6 mm and determines the Si(Li) solid angle. Each ring is equipped with 4 pins for electrical contacts welded on "lorgnettes", made of printed circuit. Measurements with an α source indicated that the total efficiency of the module equipped with the calibration telescope amounted to 70% (ring 17) to 86% (ring 14) relative to the other modules of the same ring. The electronic chains used for the calibration detectors are identical to those of the other silicon detectors. The preamplifier gains however are increased to 5 mV/MeV.

4.6. Elimination of background from scattered electrons

It is well known that a large number of electrons are emitted in the interaction of heavy ion beams with targets. Rejection of these electrons is absolutely necessary in

order to get satisfactory working conditions for the ionization chambers. The low energy thresholds required in INDRA and the 4π geometry exclude the possibility of using foils or magnets. The only practical way to reduce the noise created by the electrons relies on biasing the target with a positive high voltage. This is a very difficult task due to the short distance separating the target and the gas detectors (12 cm for rings 8 to 17). The target is mounted at the top of a 80 cm long tubular quartz rod ($\varnothing_{ext} = 15$ mm, $\varnothing_{int} = 5$ mm) which can be moved vertically (see Fig. 13). Various methods were tested to achieve the voltage transmission inside the tube. Different 80 cm long metallic wires were tested and rejected. An electrically conductive deposit on the inner wall was found to give the best results. The inner surface was frosted and covered with a thin layer of silver filled epoxy (EPO-TEK H20E-175 from Epoxy Technology). The polymerization of this two component epoxy was obtained in one hour at 150°C. The adhesion on the surface is much better than that of the silver deposit obtained through chemical methods.

The target holder allows several weeks use at 35 kV bias without breakdown. During test experiments, a maximum voltage of 55 kV was reached. However, the very high sensitivity of the ionization chamber preamplifiers is not compatible with the standard regulation of the high voltage power supply. At 40 kV, the residual signal (4 V, 17 kHz) induces a 250 mV noise (peak to peak) at the output of the ionization chamber preamplifiers. A low pass filter was introduced between the power supply and the target holder. This filter, composed of a chain of 10 resistors of 1 MΩ each and the high voltage cable capacitance ($\approx$ 300 pF for 3 m in length), has a cut-off frequency of $\approx$ 50 Hz. Thus, the 17 kHz noise emission is reduced

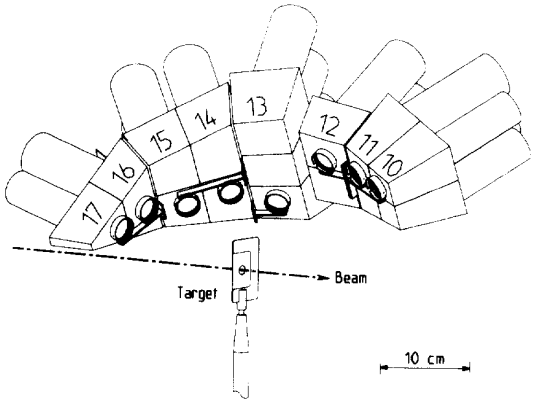

Fig. 13. Mechanical assembly of the 8 calibration telescopes and their position in front of the CsI(Tl) for rings 10 to 17. Each telescope comprises an 80 μm thick silicon detector followed by a 2 mm thick Si(Li). The target holder is also presented. The target is fixed on a thin brass plate mounted at the top of a tubular quartz rod.

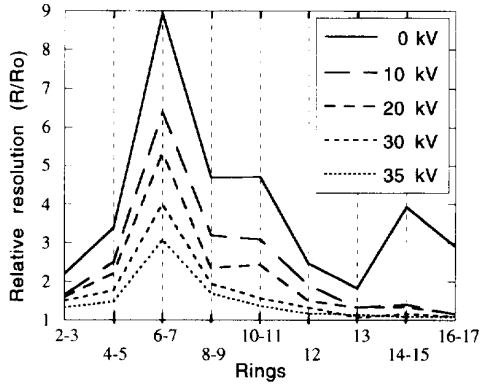

Fig. 14. Relative resolutions (R/R_0) of the ionization chambers in the presence of a 35 A MeV Kr beam (10^8 pps) on a gold target (200 μg/cm^2) and for different target bias voltages. Resolutions (R) are measured from the widths of generator pulses sent to the preamplifiers. References (R_0) correspond to measurements without beam.

by a factor of more than 300 and the nominal resolution of the ionization chambers is recovered.

In order to get information on the target bias efficiency, we checked the ionization chamber resolutions for typical experimental conditions, i.e. a 35 A MeV krypton beam of 10^8 pps impinging on a gold target (200 μg/cm^2). Reference resolutions are taken, in the absence of beam, from the width of the peaks obtained with a pulse generator on the preamplifiers. Fig. 14 presents the evolution of the resolution (normalized to the references) for different target biases in the presence of a Kr beam. The maximum degradation of the resolution is observed on the ionization chamber preamplifiers of rings 6 and 7. Even if the real yield of electrons is still unknown, this could be explained by the relatively large solid angle of these ionization chambers located at forward angles ($14° < \theta < 27°$). Nevertheless, the resolution measurements in presence of 35 A MeV Kr beam show that the target bias reduces the noise due to scattered electrons down to proportions which are compatible with the energy resolutions required for the ionization chambers.

5. Electronics and data acquisition

The detector modules have the intrinsic capacity of satisfying the required specifications concerning nucleus identifications and energy resolutions as long as a large dynamic range in energy measurements can be achieved. Furthermore, the complexity of the electronics associated with the large number of channels raises some difficulties related to its tuning, control and overall management. Consequently, a number of complementary requirements were placed on the design of the INDRA electronics and

data acquisition: i) a very low noise level and a large dynamic range, ii) a close proximity to the detector, iii) a minimum number of connectors, iv) a full software control of settings, v) a compatibility with the VME based GANIL acquisition and vi) an easy visualization of the relevant signals.

To meet these requirements the electronics had to be adapted to the specifics of the detectors and so, most of the electronic modules were designed and constructed by the collaborating laboratories. Among the particular features which contribute to the final performance level, the following should be pointed out. A particular effort was invested in the design of the reaction chamber, the detectors, the front end electronics and connections, with special care being paid to the ground reference in order to avoid crosstalk and ground loop effects. Requirements i) and ii) imply that the front end electronics (preamplifiers and PMT bases) are located inside the reaction chamber, as close as possible to the detectors. In order to fulfill these requirements, it was decided that all the electronics should be placed in the beam cave which in conjunction with items iv) and v) had important consequences concerning the choice of a new standard: the VXIbus (VME extension for instrumentation). The VXIbus [40] has been developed by a consortium of manufacturers for high quality electronic applications and compatibility with the VME computer bus. It allowed us to considerably reduce the number of modules and connections (item iii) by grouping many functions in the same module (D size: 14.4 in. × 13.4 in.). This choice also has the additional advantage of allowing the development of an easy to use and remotely controlled visualization of the signals (item vi) without cable disconnections.

This section presents the main features of the electronics and data acquisition system. A more detailed description can be found in Ref. [16].

Fig. 15 presents a general view of the electronic layout. Signals coming from the detectors are processed by two different electronic systems: one dedicated to the ionization chambers and silicon detectors, the other to scintillators. The large dynamic energy range required for the ionization chambers and silicon detectors is obtained by means of a new method. The preamplifier signal is shaped in an amplifier (consisting of 1.5 μs CR-RLC filters followed by a clamp circuit) giving a negative unipolar signal with a width (3.5 μs) which is practically independent of amplitude. The amplifiers are housed in 8 input CAMAC modules. The gain on each channel can be varied through CAMAC commands (from 0.45 to 4.7 in steps of × 1.4). The analog to digital conversion is achieved by double charge encoding: two integrators with gains in the ratio 1 : 16 and two multiplexed 12 bit converters. The "low gain" data are obtained on the full dynamic range and the "high gain" ones are provided for low energies only (1/16 of the dynamic range). These encoding functions are implemented in 32 input VXIbus modules. The

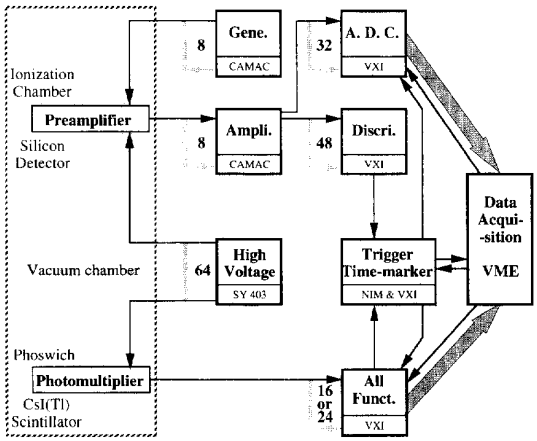

Fig. 15. Schematic representation of the main electronics functions.

CAMAC amplifier modules also deliver 8 fast outputs. These are fed to constant fraction discriminators (48 input VXIbus modules) which deliver time reference signals to the "trigger and time-marker" system and to the ADCs. In order to control the stability of the electronics, 8 output CAMAC pulse generators, including software command of amplitude, rise time and individual inhibition of the channels, were developed. The CsI(Tl) PMT signals are fed to 24 input VXIbus modules containing all the necessary processing functions. Each channel comprises a constant fraction discriminator, two integrators for fast and slow components with accompanying delay and gate generators. The analog to digital conversion is performed by two multiplexed 12 bit ADCs. All the commands are software controlled. The usual settings are: a 400 ns gate for the fast component and a 1.5 μs gate delayed by 1.6 μs for the slow one. A similar VXIbus electronic module with 16 inputs is used for the phoswich detectors. The signal is charge integrated in two different time gates: a short one (30 ns) during which the light of the fast plastic scintillator is measured and a larger one (800 ns) for the total signal.

The large number of detectors (628) imposes a specific choice for the triggering system. The standard type of trigger (master decision allowing a subsequent opening of the encoding gates) is precluded because of the requested long delays on every channel and, consequently, the analog signals may be deteriorated. A new method called "asynchronous mode" was introduced: each tagged channel stores its own analog signal in the integrators and, after a delay of 1 μs resets itself. If the event is accepted, the reset is inhibited and the stored information is digitized. The axial symmetry of INDRA led us to consider event selections based on ring dependent multiplicity levels. Each of the 336 detection cells delivers a 0.3 mA signal per hit. These individual multiplicity currents are added to form 8 independent multiplicity signals (rings 1, 2 and 3, 4

and 5, 6 and 7, 8 and 9, 10 and 11, 12 and 13, and 14–17). The triggering configuration is selected by software controlled switches on the 8 multiplicity signals. The final total multiplicity level can be adjusted from 1 to >15. This configuration can be easily modified by software through the VXIbus "selector". This module also ensures the generation of test configurations for the laser system and pulse generators which are used for stability controls (see Section 6).

Since nucleus identification relies on energy measurements, precise time measurements are not necessary. However, to estimate the importance of random coincidences, we have to know which beam pulse is associated with the trigger of any given detection cell. As at GANIL beam pulses are separated by 80 to 120 ns, a 10 ns time resolution is sufficient for this purpose. Time measurements are performed on the 628 detectors in VXIbus "time marker" modules (96 channels each) which make use of the 100 MHz clock available on the backplane of the VXIbus crate.

Except for the high voltage power supply system (8 CAEN model SY 403 crates, up to 64 independent channels per crate, [41]), the scalers (16 modules CAEN-V260, 16 channels each, [41]), the VME processors and drivers and the VXIbus controllers (STR 8032, Slot 0 from STRUCK Company, [42]), all the other electronic modules were designed and constructed by the laboratories of the INDRA collaboration. The standards were chosen in relation to software access: NIM (4 crates, no access), CAMAC (3 crates, commands only), VXIbus (4 D-size crates, commands and acquisition readout). All the electronics software accesses (commands and controls, data readout and buffer packaging) are centralized in a master VME crate.

The data acquisition rate depends on the events considered. For instance, a typical data acquisition rate of 400 events per second with a 20% dead time is obtained for multiplicity 20 events (≈ 120 parameters). The data acquisition system is the standard GANIL one [43] in which the master VME crate is connected to a central VAX 6510 computer via an optical data link. The 6510 VAX computer has a 128 megabyte central memory which allows the storage of all the control spectra: 1800 one-dimensional (512 channels each) and 1400 two-dimensional (128×128 channels). These spectra are displayed on VAX workstations. Specific programs have been developed in order to get fast access to this large number of spectra. Depending upon their size, about 150 events per second can be treated by the control task.

VXIbus permits a considerable reduction in the number of electronic modules and, consequently, the reliability of the system is greatly increased. Moreover, all the settings (thresholds, gains, timing, $\cdots$) are computer controlled. VXIbus also provides the means to introduce a standardized remote display of analog and logic signals. Under software control, the signals inside the modules can be multiplexed and accessed through 5 coaxial connectors on the VXIbus Slot0 front panel and displayed on oscilloscopes. Graphical software packages have been developed to set up parameters and select the signals to be visualized. These operations are activated from dedicated workstations. The connections to the INDRA electronics are reduced to VME-computer links (Ethernet and data optical fibers) and to a set of 20 coaxial cables (5 per VXIbus crate) for remote visualization of signals.

6. Stability controls and energy calibrations

There is no time of flight measurement in INDRA and the kinematical properties of the nuclear reactions are derived from the energy of the detected nuclei. Thus, a precise energy calibration of all detectors is mandatory. The quality of the data also relies on the validity of these calibrations over long periods of data taking, and therefore on the stability of the detectors. In this section we will first present the systems developed for stability controls, and then we will discuss the various methods used to calibrate the detectors. The calibrations take advantage of all the GANIL facilities [44] for producing high and low energy beams, as well as secondary beams of light particles and fragments. They are performed without dismounting any of the detectors.

6.1. Stability control of the silicon detectors and ionization chambers

Each preamplifier attached to the ionization chambers and to the silicon detectors is fed by signals coming from pulse generators. There is one generator output for each ionization chamber and calibration telescope channel (i.e. $96 + 16 = 112$ generators). Each silicon wafer shares the same generator signal, thus leading to 48 generator channels. During an experiment, these generators are regularly enabled by the trigger following the time sharing of the beams delivered by GANIL. In a typical arrangement, the beam arrives in the INDRA cave during 90% of a time cycle. For the remaining 10%, while the beam is directed to another experimental area, the trigger enables the pulse generators and the laser (see below) used for stability controls. The detectors and their electronic chains were found to be remarkably stable (better than 0.5%) during the first series of experiments, which ran over a period of two months.

6.2. Stability control of the scintillators

All the scintillators are connected to a laser system by means of optical fibers (Ensign–Bickford) and optical connectors (LEMO serie OB). A simplified description of the light distribution system is presented in Fig. 16. The nitrogen laser [45] is equipped with a sealed laser gas cell

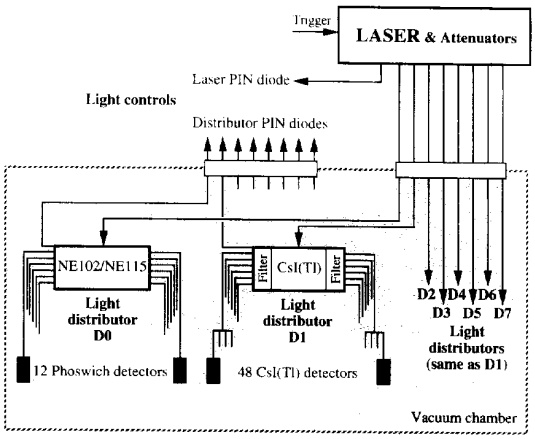

Fig. 16. Schematic lay-out of the laser distribution system.

delivering up to 20 pulses per second at a wavelength of 337 nm. The average pulse energy is 200 μJ and the peak power 70 kW. The UV laser-light is focused using a cylindrical quartz lens. From the image position the light enters a bundle of nine UV-quartz fibers (600 μm core diameter) and then traverses an attenuator (1 to 1/20) allowing variations of pulse intensities. The laser light amplitude is monitored by a PIN diode (Hamamatsu S1223) illuminated by one of the nine fibers. The eight other fibers enter the vacuum chamber and each one illuminates a small cylindrical wavelength shifter and light splitter that we call the "light distributor". A bundle of 6 quartz fibers (600 μm core diameter) is mounted on each opposite face of the cylinder. Each of these fibers, except for those of ring 1, splits up into four 200 μm core diameter individual fibers by means of connectors. These 200 μm fibers are coupled perpendicularly to the back face of the scintillators by means of small metallic connectors glued on the crystals and they illuminate a 2.5 mm diameter surface. The relative light output distribution varies within different light distributors from 4% to 8% and the total spread, σ, is of the order of 15% for the final fibers. Two types of light distributors are used. For the phoswich detectors (ring 1), we use a cylinder of NE115 (3.1 cm long – 1.5 cm diameter – optically polished) coated with a thin foil (50 μm) of NE102, which reproduces the two light components of the phoswich. The light distributor is wrapped in 500 μm teflon and housed in an aluminum box. For the other rings, the distributors are made of CsI(Tl). However, due to the large energy deposited by each laser pulse (0.5–10 TeV) in the light distributor, not only do we see the well known CsI(Tl) light components but a faster one, characteristic of the host crystal ($\approx$ 330 nm), is also observed [43]. An optical filter is therefore placed between the fiber bundles and the CsI(Tl) cylinder. This filter reduces the 330 nm light component by a factor 10^5.

The laser pulse amplitude is rather unstable: the largest amplitude and the smallest fluctuations are obtained at 10 Hz. In these conditions, fluctuations up to 8.5% were observed during a month long experiment. The stability control of all the detectors is done by monitoring each light distributor with a PIN diode which is illuminated by a thirteenth quartz fiber added to one of the bundles. The signals of the PIN diode preamplifiers are processed by the same electronics as the one used for silicon detectors, including electronic stability control by pulse generators. The light supplied by each CsI(Tl) distributor is found to be much more stable (2% variations) than the laser light itself. This is due to a saturation of the luminescence centers produced by the presence of Tl. Conversely, the 330 nm light from the host crystal, strongly suppressed by the optical filter, was found to follow the laser variations. During a two month period, 98% of the detectors were found stable to within 5%.

6.3. Energy calibration of the silicon detectors

Energy calibration of the silicon detectors for light fragments ($Z < 12$) and particles is obtained by the classical method, using precision pulse generators. The amplitude of the pulser is converted into MeV by means of a ^{212}Bi/^{212}Po α source. For the Si(Li) detectors which are not reached by the α particles of the source, the absolute energy is obtained from the secondary proton and α beams used for the calibration of the scintillators.

For heavier fragments, an absolute energy calibration of the 300 μm silicon detectors is carried out by measuring the elastic scattering of low energy (7–9 A MeV) heavy ion beams from a gold target. The beams selected (Ar, Ni, Xe) are those used in the high energy experiments, but the second GANIL cyclotron is by-passed. All the silicon detectors are thus calibrated simultaneously. In addition, for detectors located at very forward angles (rings 2 and 3), some calibration data can also be obtained from the elastic scattering of high energy heavy ion beams.

These measurements showed that for ions which punch through the silicon detectors, including nuclei as heavy as Gd, the energy is measured correctly: the pulse height defect (PHD), if any, represents less than 1% of the energy. For nuclei which stop in the silicon detectors, the PHD remains low for nuclei with atomic numbers up to 20. For 9 A MeV Ni ions, a PHD of 0.5% to 7%, depending on the wafer, is measured. These values reach 6% to 25% for 7.7 A MeV Xe ions. The PHD data are fitted with a simple power law as used for surface barrier detectors [47].

6.4. Energy calibration of the ionization chambers

Energy calibrations of the ionization chambers are performed simultaneously with those of the silicon detectors: the measurements described above (using sources and low

energy beams) are made twice, first with empty chambers, and then with the nominal gas pressures used during the experiments. The difference in the energy response of the silicon detectors gives the absolute energy lost in the ionization chambers. These values are then coupled with the data from the pulse generators which are used to obtain the linearity of the electronic chains over the whole energy range.

6.5. *Energy calibration of the scintillators*

The light response of scintillators is known to be strongly dependent on the nature of the incident particle, and is non-linear in energy. It is therefore necessary to calibrate these detectors with particles and fragments of well determined energies. For this purpose, secondary beams of light particles (mainly H and He isotopes) can be produced by the fragmentation of an intense ^{16}O beam (95 A MeV, 1.5×10^{12} pps) stopped in a thick carbon target. After momentum selection carried out with the "alpha magnetic spectrometer" of GANIL [44], secondary particles are elastically and inelastically scattered on a thick C or Ta target in the INDRA reaction chamber. The spectrometer is successively set to select magnetic rigidities corresponding to proton energies ranging from 11 to 250 MeV.

Specific calibration procedures have been dedicated to the scintillators, following their angular position in INDRA:

i) For the phoswiches, the secondary light charged particles beams are used as well as secondary beams of heavier nuclei obtained during the experiments from the high energy beams.

ii) For CsI(Tl) located below 45° (rings 2–9), the energy range obtained with the scattered secondary particles is large enough, and the calibration of the scintillators for light charged particles is thus achieved. For $Z \geq 3$ fragments, the calibration is made by using the energy loss of these nuclei in the 300 μm silicon detectors and the range-energy tables [48] for the ridge line of each element in ΔE–E maps.

iii) For the CsI(Tl) located at backward angles, the previous methods are no longer sufficient. The secondary scattered beams of H, He only furnish low energy particles (≤ 30 MeV). Thus for all nuclei the calibration relies on the calibration telescopes: the spectra obtained for each scintillator, and each nuclear species, are adjusted to those measured simultaneously on the telescopes during an experiment. Evidently, severe constraints are put on these adjustments by the few data obtained with the secondary particle beams, and with the $^{212}Bi/^{212}Po$ α source.

7. Performances

INDRA is a combination of several types of detectors designed to optimize nucleus identification over a broad energy dynamic range. The general performances depend obviously on the quality of the detectors and the associated electronics but also on the homogeneity of their response as well as on their stability over long periods of time.

A first example of the quality and uniformity of the

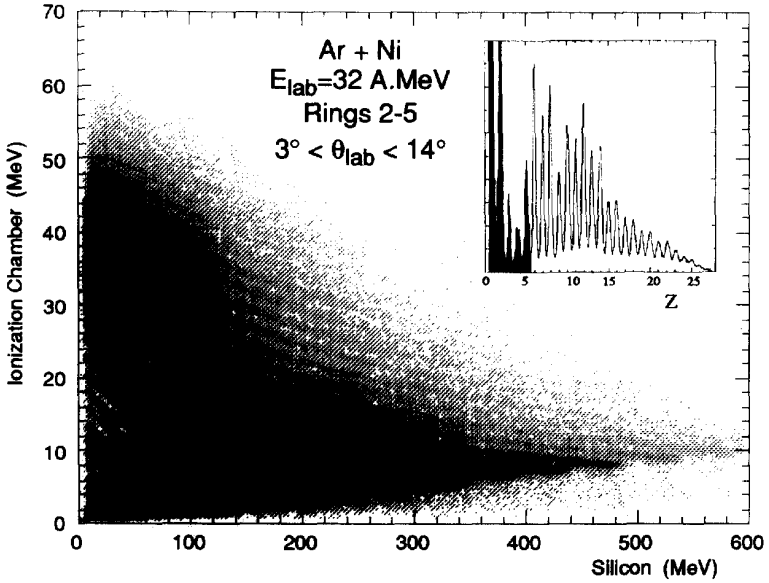

Fig. 17. ΔE–E representation (ionization chamber – silicon detector) for rings 2–5. This corresponds to the superimposition of 84 ΔE-E plots. Only particles stopping in the silicon detectors are shown. The inset shows the charge distribution obtained from identification functions.

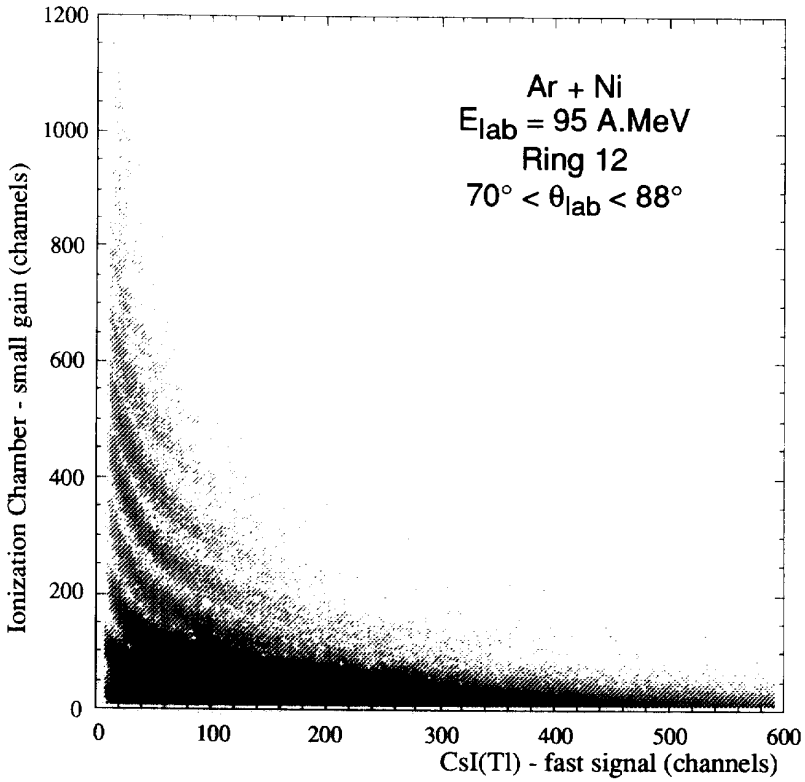

Fig. 18. ΔE–E representation (ionization chamber – CsI(Tl) detector) for ring 12. This corresponds to the superimposition of 24 ΔE–E plots.

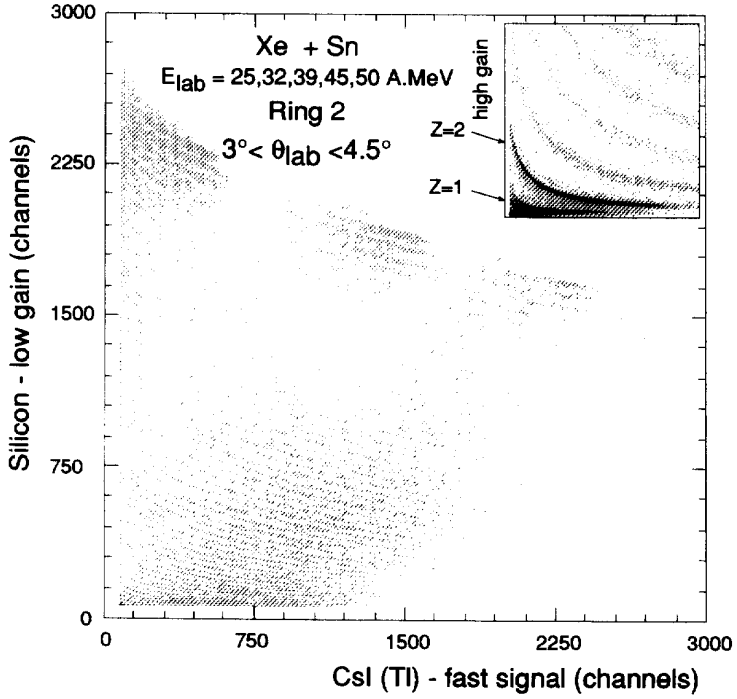

Fig. 19. ΔE–E representation of a silicon detector (low gain) of ring 2 versus the corresponding CsI(Tl) detector. The inset shows the lower energy data when the silicon high gain is used. Data obtained at different beam energies are added.

detector response is illustrated in Fig. 17 which shows the ΔE–E matrix (ionization chamber (50 mbar of C_3F_8) versus the silicon detector) obtained by superimposing the 84 modules of rings 2 to 5. The gains of the 24 ionization chambers and the 84 silicon detectors are adjusted using only pulser information. In this figure, the nuclei which punch through the 300 μm silicon detectors are rejected. Identification up to $Z = 27$ is observed even at very low energies. Events close to the ΔE axis correspond to energies of the order of 1 A MeV. Results at backward angles (ionization chambers versus CsI(Tl)) are shown in Fig. 18. In this figure, the 24 modules of ring 12 are superimposed. The gains for each module were renormalized using α particles from a ^{212}Po source. In this spectrum, low energy He nuclei are clearly separated from the background. These two examples emphasize not only the low energy thresholds in charge identification provided by the ionization chambers ($\approx$ 1 A MeV) but also the high homogeneity of the detector responses and of the associated electronics.

Fig. 19 shows the ΔE–E matrix (silicon versus CsI(Tl)) obtained from one module of ring 2. Reaction products from Xe + Sn at five bombarding energies are added. This corresponds to 60 hours of data storage without any off line gain adjustment. Excellent resolution and stability are observed and nuclei up to $Z = 54$ are identified. The inset in Fig. 19 shows the lower left corner of this matrix when the "high gain" is used for the silicon detector. A clear separation between $Z = 1$ and $Z = 2$ is observed. In certain instances, the separation of low energy hydrogen isotopes is also possible. Even if the mass identification of light particles is mainly assumed by the CsI(Tl) (see below), these results show that the identification can be extended to very low energies through the silicon detector. As the protons can lose less than 1 MeV in the silicon detector and as the electronics is set to collect up to 5 GeV, a dynamic range of more than 1 to 5000 is achieved with a resolution of 100 keV to 200 keV depending on the detectors. These features are obtained because of i) the very low background noise level (100 keV correspond to a voltage step of less than 20 μV during the opening of the ADC gate) and ii) the new method adopted for energy measurements (a low gain and low noise unipolar amplifier associated to a dual charge sensitive ADC which is equivalent to a 16 bit converter). Such an important dynamic range indicates that INDRA can be used for the study of systems with different projectile, target and incident energies without modifying the electronic settings.

Fig. 20 shows a scatter plot of the fast component as a function of the total component for one of the phoswich (NE102/NE115) detectors. The data were obtained in the measurement of the reaction ^{86}Kr + ^{27}Al at a bombarding energy of 60 A.MeV. An elemental resolution up to $Z = 37$ is achieved. The steep line close to the vertical axis is the locus of all charged products stopped in the fast NE102 plastic scintillator. As indicated in Section 4.4 and dis-

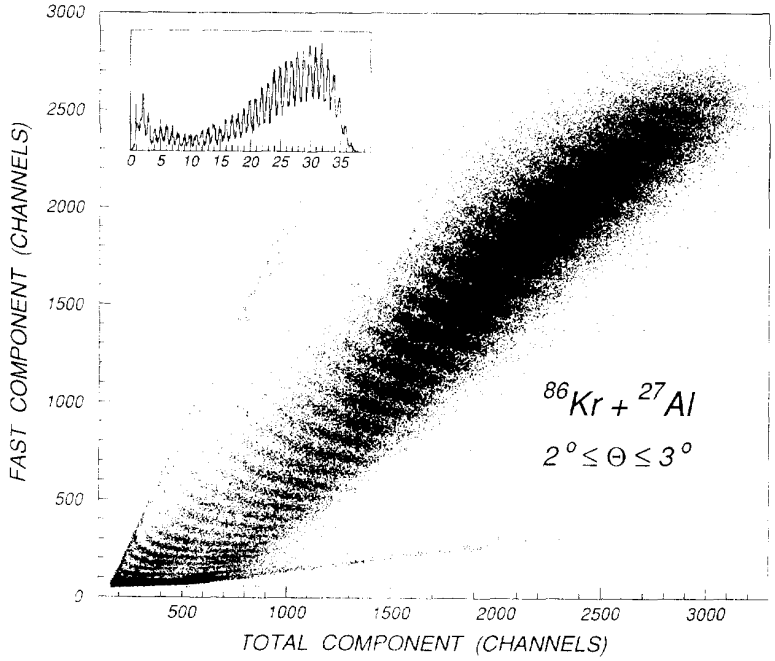

Fig. 20. Fast–total representation of a phoswich detector. The inset shows the associated charge distribution obtained from identification functions.

cussed in Ref. [37], this corresponds to energy thresholds which are higher than the ones encountered in the other INDRA detection modules (from 6.3 A MeV for H and He to 23 A MeV for Kr). The results with other beams and energies show that the charge identification is preserved even in the presence of an important flux of elastically scattered ions.

Results of particle identification for the CsI(Tl) detectors, in the fast–slow representation, are shown in Figs. 21 and 22. The former shows the results obtained for ring 3 where mass and charge identifications up to $Z = 5$ are observed. The lower inset shows the improvement in the isotopic separation for low energies when the high gain signal of the associated silicon detector is added to the fast component. For very thick detectors, as those used in the forward rings, fast neutrons have a significant probability of interacting with the medium through nuclear reactions. The resulting charged particles, mostly slow protons and α particles, are detected and can be identified by the absence of an energy loss signal in the associated silicon detector. The upper inset shows the identification function obtained for this spectrum when a signal in the associated silicon detector is required. Ghost identification peaks are visible, originating from the pile up of 2 protons and 2 α particles. The second peak can mainly be attributed to the ^{8}Be decay. Fig. 22 shows similar results for a CsI(Tl) detector of ring 10. The inset shows the excellent separation between particles close to the detection threshold and the energy calibration obtained both for protons and α particles. The separation between $Z = 1$ and $Z = 2$ is performed for energies greater than 2 MeV for H particles (4 MeV for He). The separation between protons and the other H isotopes is obtained for an energy greater than 5 MeV. Due to the setting of the photomultiplier gain, the energy thresholds for charge and mass identifications of light particles with the CsI(Tl) detectors vary from ring to ring. In Figs. 21 and 22, although the totality of the spectra are not presented (4096 × 4096 channels in the original two-dimensional spectra), no problems are encountered for high energy particles as the detector thicknesses are large enough to stop nearly all the particles emitted (see Table 2).

Fig. 23 shows the resolution obtained with the calibration detectors (silicon 80 μm and Si(Li) 2 mm) of ring 10.

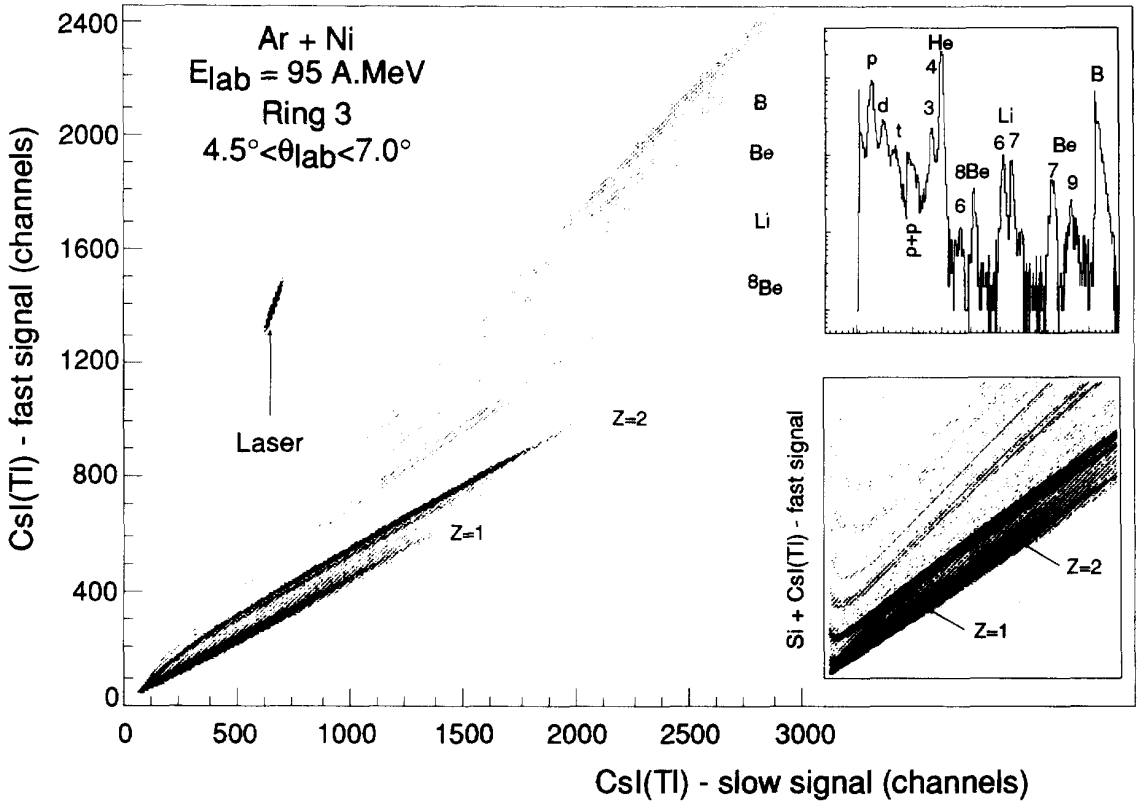

Fig. 21. Fast–slow representation of a CsI(Tl) detector of ring 3. The lower inset shows the improvement of the charge separation obtained at low energies when the high gain signal of the associated silicon detector is added to the fast component. Upper inset shows the identification function.

The events punching through the Si(Li) detector have been removed. Isotopic separation is achieved up to boron. The inset of this figure shows the light particle identification region where the sharpness of the "cuts" indicates the homogeneity of the thickness of the Si(Li) detector. The quality of the telescope allows to perform an energy calibration of the corresponding CsI(Tl) detector. The extension to the other detectors of the same ring relies on their uniformity. Fig. 24 shows the dispersion in counting rate obtained for protons in ring 10. The shaded area corresponds to a fluctuation of $\pm 5\%$ and the dip for module no. 2 corresponds to the presence of the calibration detector. This example clearly shows that the counting rate is the same for all the detectors in the ring.

A more general result is given by Fig. 25 in which the charged product multiplicity distributions obtained for the reactions $^{36}Ar + ^{58}Ni$ and $^{129}Xe + ^{nat.}Sn$ are presented. Multiplicities up to 50 are measured and, correcting for efficiency and multi-hit probability, these would correspond to an initial multiplicity of about 55. The possibility to record efficiently events with such high charged product multiplicities comes from the excellent spatial coverage (90% of the 4π solid angle) as well as from an appropriate angular segmentation (see Sections 2 and 3).

All the results presented in this section are extracted from the data recorded in March and April 1993 during the first set of experiments performed with argon, krypton, xenon and gadolinium beams bombarding various targets. They can be considered as the typical results of the INDRA set up, which is thus one of the most efficient detectors of its type. Some features are also important as they permit simplification of the data analysis. For instance, the large energy dynamic range allows us to run all the experiments without changing the electronic gains of the amplifiers (ionization chambers and silicon detectors) and the high voltage bias of the photomultipliers (scintillators). Thus, the comparison and simultaneous analysis of the results with different beams, targets and incident energies are largely facilitated. However, the number of detection cells, and hence the variety of identification matrices to consider, remains important and a significant effort has been made in data analysis. Automatic or semi-automatic identification procedures, such as the ones presented in Ref. [49], have been developed. This was possible only

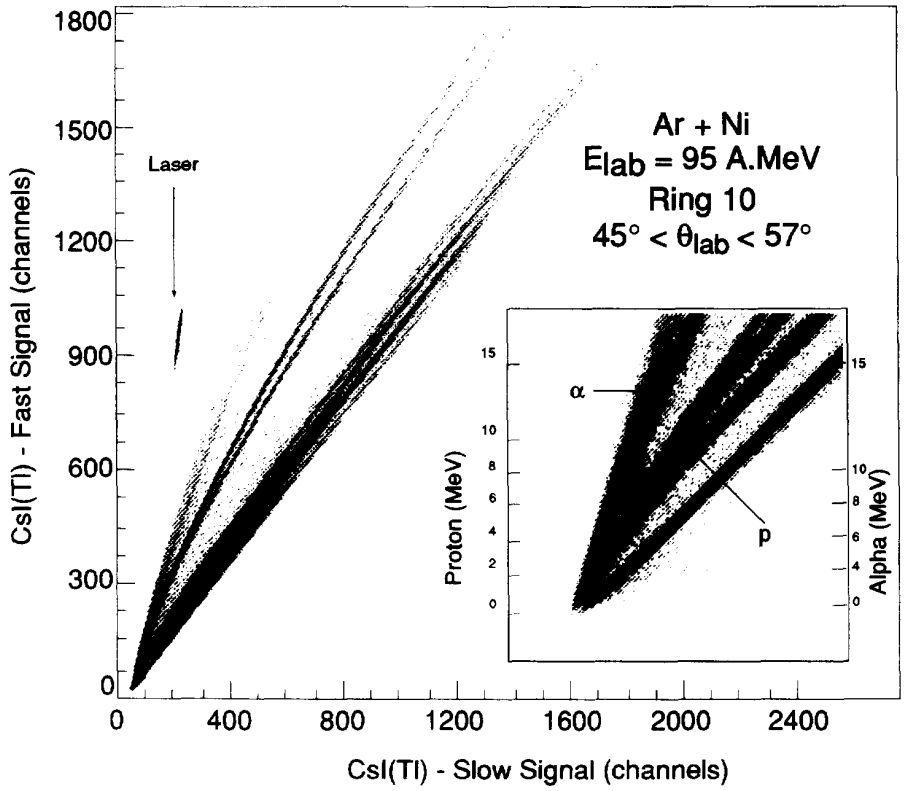

Fig. 22. Fast–slow representation of a CsI(Tl) of ring 10. The inset shows the isotopic separation achieved at low energies and calibrations corresponding to protons and α particles.

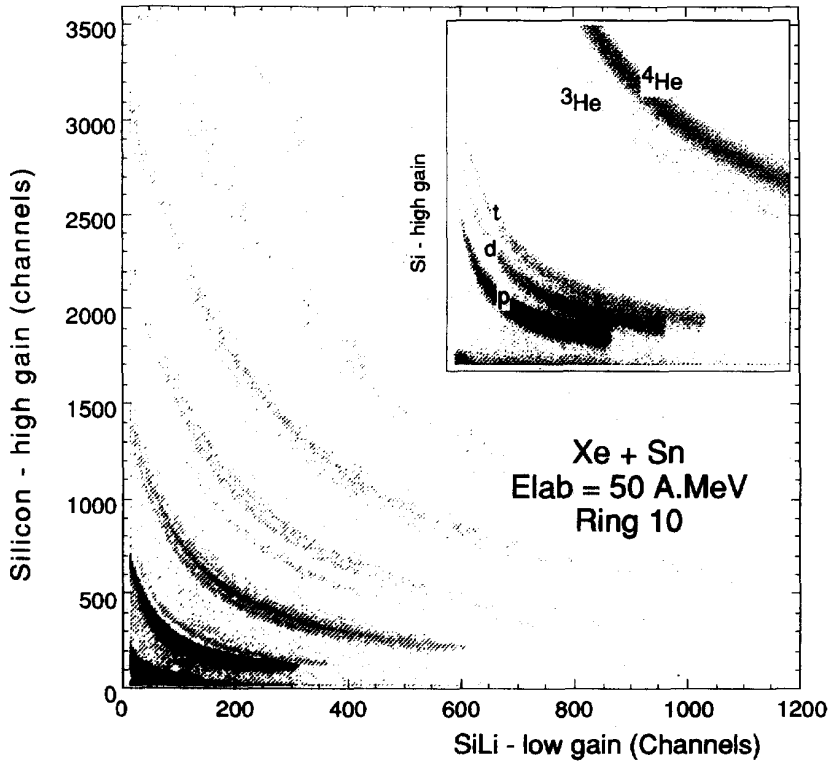

Fig. 23. ΔE–E representation of the calibration telescope (80 μm silicon versus 2 mm Si(Li)) of ring 10. Only the particles which do not punch through the Si(Li) are shown. The inset shows the isotopic separation for H and He nuclei.

because of the quality, the stability and the uniformity of the detectors and the associated electronics.

Acknowledgements

The work described in this paper would have been impossible without the outstanding technical support provided by the staffs of the five laboratories involved in the INDRA project. We particularly wish to thank M. Fermé for useful and stimulating discussions about the high voltage bias of the target. We are grateful to the staff of the

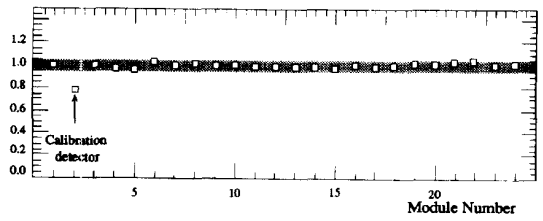

Fig. 24. Counting rates obtained for protons in ring 10. The shaded area shows fluctuations of ±5%. The dip for module 2 corresponds to the presence of the calibration detector of this ring.

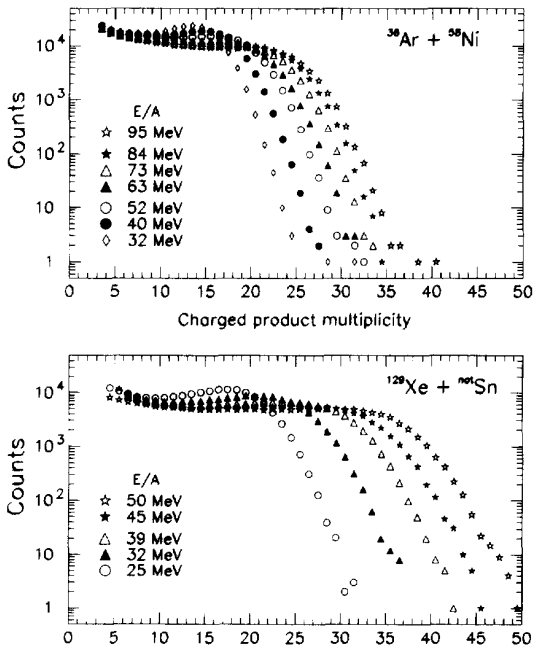

Fig. 25. Examples of charged product multiplicity distributions. Events were recorded when at least N modules of INDRA fired ($N = 3$ for 32–73 A MeV Ar beams and $N = 4$ otherwise).

GANIL accelerator for their precious support during our test and experiment periods. The first tests of the ionization chamber arrays were performed on the Saclay Tandem-Booster and we have enjoyed the excellent services of the accelerator crew. We are also indebted to Y. El Masri, F. Hanappe and J. Guillot for their friendly and efficient involvement during the tests of the CsI(Tl) and the calibration of the Si(Li) detectors in Louvain-la-Neuve and Orsay. We would like to thank J.L. Altier (J.L.A. Ingenierie Company) for the careful realisation of the laser and light distribution system. We are grateful to E. Kashy and M. Mac Cormick for their careful reading of the manuscript.

References

[1] L.G. Moretto and G.J. Wozniak, Ann. Rev. Nucl. Part. Sci. 43 (1993) 379, and references therein.
[2] J. Cugnon, Phys. Lett. B 135 (1984) 374.
[3] C.J. Pethick and D.G. Ravenhall, Nucl. Phys. A 471 (1987) 19c;
H. Heiselberg, C.J. Pethick and D.G. Ravenhall, Phys. Rev. Lett. 61 (1988) 818.
[4] G.F. Bertsch and Ph. Siemens, Phys. Lett. B 126 (1989) 9.
[5] E. Suraud, D. Cussol, Ch. Gregoire, D. Boilley, M. Pi, P. Schuck, B. Remaud and F. Sebille, Nucl. Phys. A 495 (1989) 73c.
[6] G.D. Westfall, J.E. Yurkon, J. Van der Plicht, Z.M. Koenig, B.V. Jacak, R. Fox, G.M. Crawley, M.R. Maier, B.E. Hasselquist, R.S. Tickle and D. Horn, Nucl. Instr. and Meth. A 238 (1985) 347.
[7] G. Bizard, A. Drouet, F. Lefebvres, J.P. Patry, B. Tamain, F. Guilbault and C. Lebrun, Nucl. Instr. and Meth. A 244 (1986) 483;
R. Bougault, J. Duchon, J.M. Gautier, A. Genoux-Lubain, C. Lebrun, J.F. Lecolley, F. Lefebvres, M. Louvel, P. Mosrin and R. Regimbart, Nucl. Instr. and Meth. A 259 (1987) 473;
A. Péghaire, B. Zwieglinski, E. Rosato, G.M. Jin, J. Kasagi, H. Doubre, J. Péter, F. Guilbault, C. Lebrun, Y. Cassagnou and R. Legrain, Nucl. Instr. and Meth. A 295 (1990) 365;
G. Rudolf, J.C. Adloff, R. Bilwes, F. Cosmo, M. Glaser, A. Kamili, F. Scheibling and L. Stuttgé, Nucl. Instr. and Meth. A 307 (1991) 325.
[8] D.G. Sarantites, L.G. Sobotka, T.M. Semkow, V. Abenante, J. Elson, J.T. Hood, Z. Li, N.G. Nicolis, D.W. Stracener and J. Valdes, Nucl. Instr. and Meth. A 264 (1988) 319;
D.W. Stracener, D.G. Sarantites, L.G. Sobotka, J. Elson, J.T. Hood, Z. Majka, V. Abenante, A. Chbihi and D.C. Hensley, Nucl. Instr. and Meth. A 294 (1990) 485.
[9] AMPHORA Collaboration: D. Drain et al., Nucl. Instr. and Meth. A 281 (1989) 528.
[10] R.T. DeSouza, N. Carlin, Y.D. Kim, J. Ottarson, L. Phair, D.R. Bowman, C.K. Gelbke, W.G. Gong, W.G. Lynch, R.A. Pelak, T. Peterson, G. Poggi, M.B. Tsang and H.M. Xu, Nucl. Instr. and Meth. A 295 (1990) 109.
[11] A. Gobbi et al., Nucl. Instr. and Meth. A 324 (1993) 156.
[12] E. Migneco, C. Agodi, R. Alba, G. Bellia, R. Coniglione, A. Del Zoppo, P. Finocchiaro, C. Maiolino, P. Piattelli, G. Raia and P. Sapienza, Nucl. Instr. and Meth. A 314 (1992) 31.
[13] J. Galin et al., Proc. Int. Conf. on New Nuclear Physics with Advanced Techniques, Ierapetra, Greece (World Scientific, 1992) p. 131.
[14] J. Alarja, A. Dauchy, A. Giorni, C. Morand, E. Pollacco, P. Stassi, R. Billerey, B. Chambon, B. Cheynis, D. Drain and C. Pastor, Nucl. Instr. and Meth. A 242 (1986) 352.
[15] J. Pouthas, R. Dayras, E. Plagnol, E.C. Pollacco, J.C. Roynette, F. Saint Laurent and J.C. Steckmeyer, GANIL R 88-02.
[16] J. Pouthas et al., Electronics for the INDRA 4π detection array, in preparation, to be submitted to Nucl. Instr. and Meth.
[17] G.B. Hagemann, R. Broda, B. Herskind, M. Ishihara, S. Ogaza and H. Ryde, Nucl. Phys. A 245 (1975) 166.
[18] L. Westerberg, D.G. Sarantites, R. Lovett, J.T. Hood, J.H. Barker, C.M. Currie and N. Mullani, Nucl. Instr. and Meth. 145 (1977) 295.
[19] S.Y. Van der Werf, Nucl. Instr. and Meth. 153 (1978) 221.
[20] D. Guinet, B. Chambon, B. Cheynis, A. Demeyer, D. Drain, X.C. Hu, C. Pastor, L. Vagneron, K. Zaid, D. Heuer, A. Lleres and J.B. Viano, LYCEN 8903.
[21] C.A.D. Euclide from Matra Datavision.
[22] D. Williams, G.F. Snelling and J. Pickup, Nucl. Instr. and Meth. 39 (1966) 141.
[23] E. Norbeck, R. Dayras, C. Mazur, E.C. Pollacco, D. Swan and J.X. Zhang, Nucl. Instr. and Meth. A 314 (1992) 620.
[24] Eurisys Mesures (formerly Intertechnique), 1 Parc des Tanneries, 67380 Lingolsheim, France.
[25] J. Kemmer, Nucl. Instr. and Meth. A 226 (1984) 89.
[26] N. Copinet, Ph.D. thesis, University of Caen, 1990 (unpublished).
[27] P. Dreier, Nucl. Instr. and Meth. A 288 (1990) 272.
[28] F.Z. Henari, E.C. Finch and C.F.G. Delaney, Nucl. Instr. and Meth. A 288 (1990) 439.
[29] K.J. Rawlings, Nucl. Instr. and Meth. A 291 (1990) 607, and references therein.
[30] M. Ogihara, Y. Nagashima, W. Galster and T. Mikumo, Nucl. Instr. and Meth. A 251 (1986) 313, and references therein.
[31] GUIDE7 (Version 1982), T. Massam, CERN 76-21, Exp. Phys. Div.
[32] BDH-Merck Ltd, West Quay Rd, Poole, BH15 1HX, England.
[33] Philips Photonics, F19108 Brive, France.
[34] J. Pouliot, Y. Chan, A. Dacal, A. Harmon, R. Knop, M.E. Ortiz, E. Plagnol and R.G. Stokstad, Nucl. Instr. and Meth. A 270 (1988) 69.
[35] Nuclear Enterprises Ltd, Sighthill, Edinburgh, Scotland.
[36] K.M. Teh, D. Shapira, B.L. Burks, R.L. Varner, J.L. Blankenship, E.J. Ludwig, R.E. Fauber and C.F. Maguire, Nucl. Instr. and Meth. A 254 (1987) 600.
[37] J.C. Steckmeyer et al., LPCC 94-13, submitted to Nucl. Instr. and Meth.
[38] GEANT 3: R. Brun, F. Bruyant and A.C. Mc Pherson, CERN-DD/EE/84-1.
[39] L. Stab, Nucl. Instr. and Meth. A 288 (1990) 24.
[40] VXIbus System Specification, revision 1.3, July 1989, authorized by the VXIbus Consortium Inc.
[41] C.A.E.N, Via Vetraia 11, 55049 Viareggio, Italy.
[42] Dr. B. Struck, Postfach 1261, D-2000 Tangstedt/Hamburg, Germany.

[43] B. Raine, M. Tripon and B. Piquet, GANIL A 93 01, presented at the 8th Conf. on Real Time Computer Applications in Nuclear, Particle and Plasma Physics, Vancouver, Canada, June 1993.
[44] J. Fermé, M. Gouttefangeas and the GANIL group, Proc. 9th Int. Conf. on Cyclotrons, Caen, France (Les Editions de Physique, 1982) p. 3.
[45] Laser Science Inc., Cambridge, MA, USA.
[46] R. Gwin and R.B. Murray, Phys. Rev. 131 (1963) 508.
[47] J.B. Moulton, J.E. Stephenson, R.P. Schmitt and J.B. Wozniak, Nucl. Instr. and Meth. A 157 (1978) 325.
[48] F. Hubert, R. Bimbot and H. Gauvin, Atom. Data Nucl. Data Tables 46 (1990) 1.
[49] A. Benkirane, G. Auger, D. Bloyet, A. Chbihi and E. Plagnol, GANIL P 94 20; Nucl. Instr. and Meth, in press.